Hot carrier photovoltaics in van der Waals heterostructures

Kamal Kumar Paul[1,2], Ji-Hee Kim[1,2]✉ and Young Hee Lee [1,2,3]✉

Abstract | Successfully designing an ideal solar cell requires an understanding of the fundamental physics of photoexcited hot carriers (HCs) and the underlying mechanism of unique photovoltaic performance. Harnessing photoexcited HCs offers the potential to exceed the thermodynamic limit of power conversion efficiency, although major loss channels employing ultrafast thermalization of HCs severely restrict their utilization in conventional bulk-absorber-based solar cells. Spatially confined semiconductors, especially 2D van der Waals (vdW) materials, offer several advantages, such as strong Coulomb interaction, high exciton binding energy, strong carrier–carrier scattering and weak carrier–phonon coupling, resulting in slow HC cooling and restricted loss channels. This Review provides a detailed mechanistic understanding of the HC cooling dynamics in confined vdW layered materials for efficiently utilizing HCs and discusses the role of carrier multiplication in designing a solar cell with the power conversion efficiency exceeding the Shockley–Queisser limit. Additionally, we analyse the major energy loss channels that limit the efficiency of a conventional solar cell, as well as the promises held by the 2D vdW heterostructures for an efficient HC solar cell. Furthermore, we highlight the challenges and opportunities involved in successfully utilizing HCs in practical solar cells with efficiencies beyond the thermodynamic limit.

Tandem cells
High-performance multijunction photovoltaic devices that sequentially absorb wide-range solar energy.

Carrier multiplication
(CM). Interband carrier–carrier scattering increasing the overall carrier density in the conduction band, also referred to as inverse Auger recombination.

[1]IBS Center for Integrated Nanostructure Physics (CINAP), Institute for Basic Science, Suwon, South Korea.

[2]Department of Energy Science, Sungkyunkwan University, Suwon, South Korea.

[3]Department of Physics, Sungkyunkwan University, Suwon, South Korea.

✉e-mail: kimj@skku.edu; leeyoung@skku.edu

To design an ideal solar cell, it is essential to understand the major energy loss mechanisms in a conventional solar cell. In principle, extrinsic losses (impurities, series resistance and solar absorption in inactive layers) can be eliminated by choosing proper device components and structure. However, optimizing these properties does not necessarily eliminate the intrinsic losses associated with the fundamental limitations of energy conversion (FIG. 1a). Transparency (~25%) and thermalization (~30%) losses, the two highest intrinsic energy loss channels, arise from solar energies being lower and higher than the absorber bandgap, respectively[1–3]. High energy carriers beyond the band edges that are not in thermal equilibrium with the lattice are referred to as hot carriers (HCs), which exhibit rapid relaxation via carrier–phonon scattering in a sub-picosecond timescale before arriving at the band edges for extraction. The aforementioned energy losses set a maximum thermodynamic limit of ~34% for a ~1.3-eV bandgap at 1 sun AM1.5 for the solar to electric power conversion efficiency (PCE), also termed the Shockley–Queisser (SQ) limit[4].

To overcome the SQ limit, the most dominant loss channels need to be minimized. Tandem cells may partially restrict the aforementioned loss channels and result in a high PCE (~44%)[5]. However, the fabrication of these cells is still limited in group III–V semiconductors and the fabrication cost is also high, which limits their commercial applications[6]. Several novel concepts have been able to minimize the fundamental loss channels[1,2,7–9] by generating either additional free energy (high open-circuit voltage (V_{OC})) in hot carrier solar cells (HCSCs) or free carriers (high short-circuit current (I_{SC})) in carrier multiplication (CM) solar cells[10] (FIG. 1b). The concept of HCSCs is essentially based on HCs, which can be extracted to the energy-selective contacts (ESCs) before cooling to their band edges, thereby, enhancing the PCE up to ~67%[6,9] (FIG. 1c). An alternative technique to generating HCs with below-bandgap optical excitations is an intermediate-band solar cell, which functions by multiphoton excitations through a special narrow-bandgap material introduced between the fundamental gap of absorber[11] (FIG. 1b).

A CM solar cell uses the excess energy ($E_{photon} - E_{bandgap}$) of HCs and generates additional carriers, owing to the predominant interband carrier–carrier scattering (inverse Auger process). This phenomenon was first reported in bulk semiconductors (Si and Ge with threshold energy at least twice the bandgap) and referred to as impact ionization[4,12–14]. Semiconductor nanocrystals were later demonstrated with more possibilities and termed as CM and led to an enhanced PCE[4,15,16]. Another promising

- Photogenerated hot carriers can be harnessed in spatially confined photovoltaic materials (2D van der Waals heterostructures), owing to slow hot carrier cooling and restricted loss channels, resulting in power conversion efficiency beyond the Shockley–Queisser limit.

- Weak optical absorbance of graphene can be compensated by integrating with 2D van der Waals layered semiconductors yielding relatively high absorbance. Subsequently, the enhanced photocarrier density invokes the hot-phonon bottleneck effect, leading to prolonged hot carrier cooling in graphene, which results in the synergistic hot-carrier-driven photovoltaic performance.

- Unlike conventional bulk heterostructures, direct interlayer hot carrier transfer on the ultrafast timescale can be efficient in van der Waals heterostructures without phonon emission due to momentum conservation at the K-point.

- In graphene-based 2D van der Waals heterostructures, graphene can serve as both the injector and the collector of quasi-thermalized hot carriers with high quantum efficiency.

- Both 2D van der Waals layered materials and perovskite nanostructures demonstrate high carrier multiplication conversion efficiency. Moreover, 2D van der Waals heterostructures also demonstrate highly efficient interlayer carrier multiplication near room temperature.

- van der Waals heterostructure stacking with a hot carrier absorber material, perovskite nanostructures, may offer synergistic hot carrier and carrier multiplication effects, which lead to the enhanced solar cell performance (maximum open-circuit voltage (V_{OC}^{HC}) and short-circuit current (I_{SC}^{CM})).

approach to expand the PCE is exploring the excess energy in HCs for ultraviolet-to-infrared photovoltaic shapers (FIG. 1b). A standard Si solar cell integrated with an additional SiO_2 active layer co-doped with Si nanocrystals and Er^{3+} ions converts each ultraviolet photon into multiple infrared photons with a relatively higher quantum efficiency[17].

Ideally, a HC absorber is required to have low bandgap to harvest the maximum possible solar spectrum, generate sufficient HCs and to ensure high carrier mobility, strong Coulomb interaction, slow carrier recombination and fast extraction. A few bulk materials such as GaAs[18], InN[19], GaN and BiN with high carrier mobility and phononic bandgap meet the requirements of a HC absorber, owing to the formation of a hot-phonon bottleneck. The hot-phonon bottleneck is where the relaxation rate of a nonequilibrium carrier–phonon system is reduced with high carrier injection, limiting further energy redistribution into the lattice[20]. However, realizing a practical HC photovoltaic device with bulk materials has been ineffective so far, due to poor phonon bottleneck effect upon solar irradiation having relatively low carrier concentration, as well as low material quality and challenging fabrication processes[21]. Furthermore, bulk semiconductors suffer from a low density of final states constrained by the momentum conservation principle, resulting in a high threshold energy for CM ($\geq 4E_{bandgap}$)[22–24]. However, with the integration of suitable ESCs (for electrons: TiO_2 (REF.[25]), CeO_2 (REF.[26]), SnO_2 (REF.[27]), C_{60} (REF.[28]) and Si/SiO_2 (REF.[29]); for holes: MoO_x (REF.[30]), NiO_x (REF.[31]), $NiMgO_x$ (REF.[32]), Cu_xO[33] and $CuGaO_2$ (REF.[34])), HC extraction may be improved, along with a fast charge transfer rate, resulting in an enhanced V_{OC} (REFS[35–38]).

The scenario is different in spatially confined semiconductors such as quantum dots, carbon nanotubes, nanowires and 2D van der Waals (vdW) layered materials because of strong Coulomb interaction, high

exciton binding energy, reduced charge screening and low electron–phonon coupling, leading to a slower HC cooling[24,39–42]. The quantum confinement effect relaxes the strict momentum conservation requirement for optical transition through Heisenberg's uncertainty principle, leading to a high indirect band-to-band transition and slow carrier relaxation, which results in efficient CM[23,43–47]. A number of low-dimensional materials have been demonstrated with considerably high HC and CM effects in practical devices, such as graphene[48], carbon nanotubes[49], PbS[50,51] and PbSe[52,53], CdSe[54], PbTe[55], perovskites[56,57] and many other confined structures, including $MoTe_2$ (REF.[24]), are still at the core of intensive research. 2D vdW layered material ($2H$-$MoTe_2$) demonstrates a CM conversion efficiency of ~99%, which is higher than that of quantum dots[24]. Atomically thin vdW materials (MoS_2, $MoSe_2$, WS_2, etc.) exhibit a considerably high solar light absorbance (up to 5–10%[58]), which is one order of magnitude larger than the most common photovoltaic materials (Si, GaAs, etc.)[59].

The use of vdW materials and related heterostructures in solar cells plays an important role for new physical insights and next-generation technologies. For example, designed vdW heterostructures offer strong optical absorbance in a broad energy range, effective transport and efficient interfacial carrier extraction (type II or quasi-type II junction), which are beneficial for ideal photovoltaics. Relatively high optical absorbance from the graphene–vdW transition metal dichalcogenides (TMDs) heterostructure can be obtained by compensating weak optical absorbance in graphene layers. Subsequently, the enhanced photocarrier density invokes the hot-phonon bottleneck effect, leading to prolonged HC cooling in graphene[60]. Moreover, direct interlayer HC transfer can be more efficient in vdW heterostructures than in conventional bulk heterostructures, as there is no phonon emission, owing to momentum conservation at the K-point[61]. Ultrafast formation of interlayer HCs can be facilitated efficiently in TMD–TMD vdW heterostructures[42]. These characteristics including high optical absorbance, strong hot-phonon bottleneck effect, retarded HC cooling[60], high CM conversion efficiency[24], good HC transport[62] and high carrier extraction efficiency[63] are certainly advantageous for the fabrication of efficient HCSCs. Interestingly, perovskite as a newly emerging material is another promising class of HC absorber material similar to vdW materials[56,64–66]. In this context, the combination of vdW materials with perovskites (perovskite-based vdW heterostructures) may offer synergistic HC and CM effects, leading to enhanced HCSC performance. These related heterostructures have rarely been explored for HC and CM photovoltaic effects.

In this Review, we first provide a brief overview of energy loss processes in a conventional solar cell, followed by the feasible strategies to increase the PCE. Next, we discuss the reports on bulk HC absorbers and the advantages of spatially confined semiconductors. Further, we discuss the HC dynamics in quantum-confined vdW layered materials and their heterostructures to explore an efficient HC extraction strategy. Subsequently, we discuss the recent advances
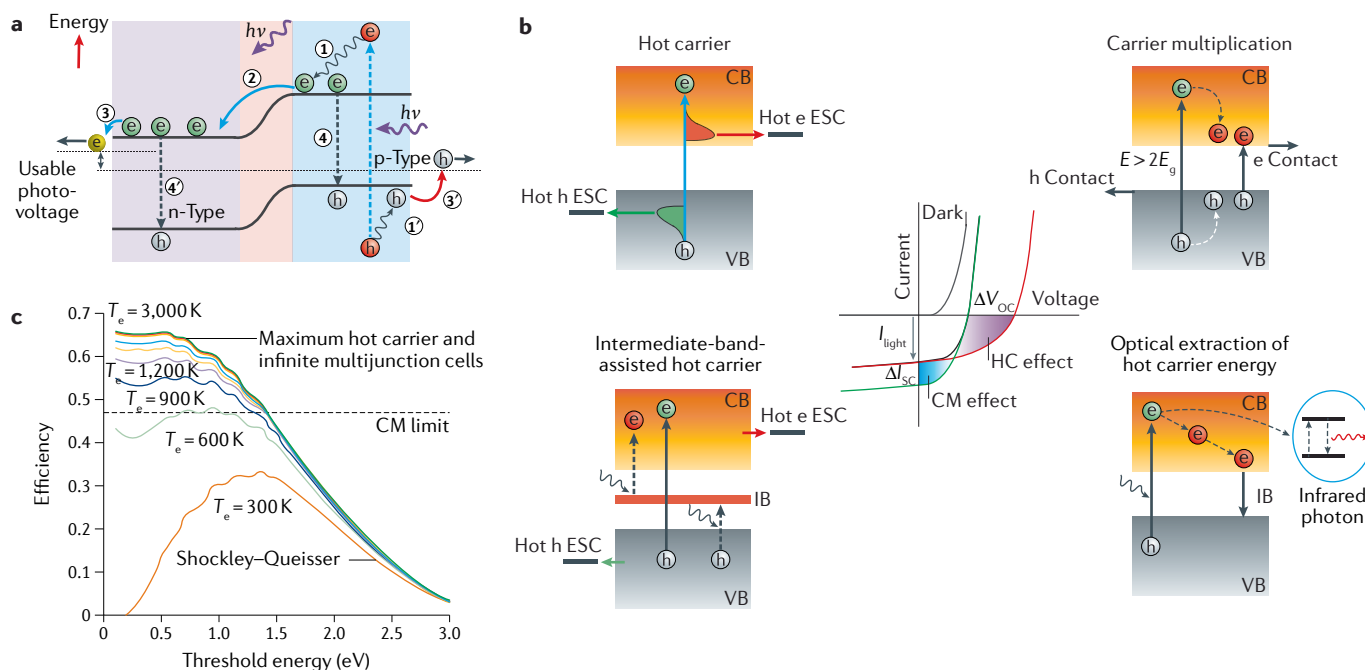
Fig. 1 | **Concept of a next-generation solar cell beyond the Shockley–Queisser limit. a** | Primary energy loss pathways in a conventional single-junction solar cell: (1, 1′) hot carrier (HC) cooling loss; (2) junction loss; (3, 3′) contact loss; and (4, 4′) recombination loss[9]. **b** | Four promising strategies for a high-efficiency solar cell assisted with HC and carrier multiplication (CM) effects. Extraction of HCs using proper energy-selective contacts (ESCs) (top left), CM (top right), absorption through an intermediate band (IB) (bottom left) and optical extraction, i.e. energy transfer from HCs to Er^{3+} ions and subsequent emission of infrared photons (bottom right). I–V curves for a conventional solar cell with HC and CM effects separately (centre). **c** | Detailed calculation for the power conversion efficiency of an ideal p–n junction HC solar cell as a function of absorber bandgap at various carrier temperatures under 1 sun irradiation[6]. CB, conduction band; OC, open circuit; SC, short circuit; VB, valence band. Panel **a** adapted with permission from REF.[9], Wiley. Panel **c** adapted from REF.[6], Springer Nature Limited.

in HC photovoltaics in vdW heterostructures. Finally, we conclude with a discussion of the challenges and opportunities for future HC photovoltaics.

HC dynamics in semiconductors

The evolution of carrier distribution with time and typical energy loss mechanism in a semiconductor through phonon decay is discussed in this section (FIG. 2a–c), followed by a list of beneficial parameters for an efficient HC absorber.

HC cooling

Upon illumination with an above-bandgap pulsed laser, charge carriers (electrons and holes) are created at the elevated positions in the respective bands of semiconducting absorber (FIG. 2a, step 1). These carriers finally establish thermal equilibrium with the lattice after the redistribution of excess energy and relaxation via various pathways. The carriers first set an equilibrium among themselves through elastic carrier–carrier scattering (steps 2 and 3) within a short time frame, τ_{th} ~100 fs; this phenomenon is called carrier thermalization. Eventually, this carrier distribution satisfies the Fermi–Dirac statistics; the carrier temperatures (T_e and T_h) are much higher than the lattice temperature (T_L), and are, thus, called HCs. Following the thermalization, HCs successively interact with the lattice mainly through phonons — inelastic carrier–phonon interactions — which decreases

their excess energy and establishes a thermal equilibrium with the lattice ($T_{e,h} = T_L$) (FIG. 2a,b). This process is known as cooling or relaxation of HCs, and the required relaxation/cooling time (τ_{re}) typically extends up to 1 ps (REF.[2]) (FIG. 2a, step 4). Generally, nonpolar materials predominantly exhibit potential deformation interactions, which involve transitory charges in the net covalent bonds, leading to weak electron–phonon interactions. In contrast, carrier–phonon interactions predominantly occur in polar materials through Fröhlich interactions (carrier–longitudinal optical (LO) phonon scattering), which is one of the most dominant relaxation pathways for HCs (FIG. 2b). HC relaxation occurs in three aforementioned steps, and any interruption leads to the slowing down of cooling. Fröhlich interactions (first step) can be blocked by changing the bond polarization, whereas decay of optical phonons into acoustic modes (second step) can be tuned by the formation of a phonon bottleneck. The nonequilibrium acoustic phonons (third step) developed after the optical phonon decay also contribute to lowering the HC cooling[67,68].

Phonon decay mechanism

HC cooling via LO phonon emission in the presence of a phonon bottleneck restricts the redistribution of LO phonon energy into the acoustic phonons, leading to the rapid formation of a nonequilibrium population of hot phonons at a narrow region of the decay cascade

Decay cascade
When a LO phonon decays its energy by successive emission of multiple optical and acoustic phonons.
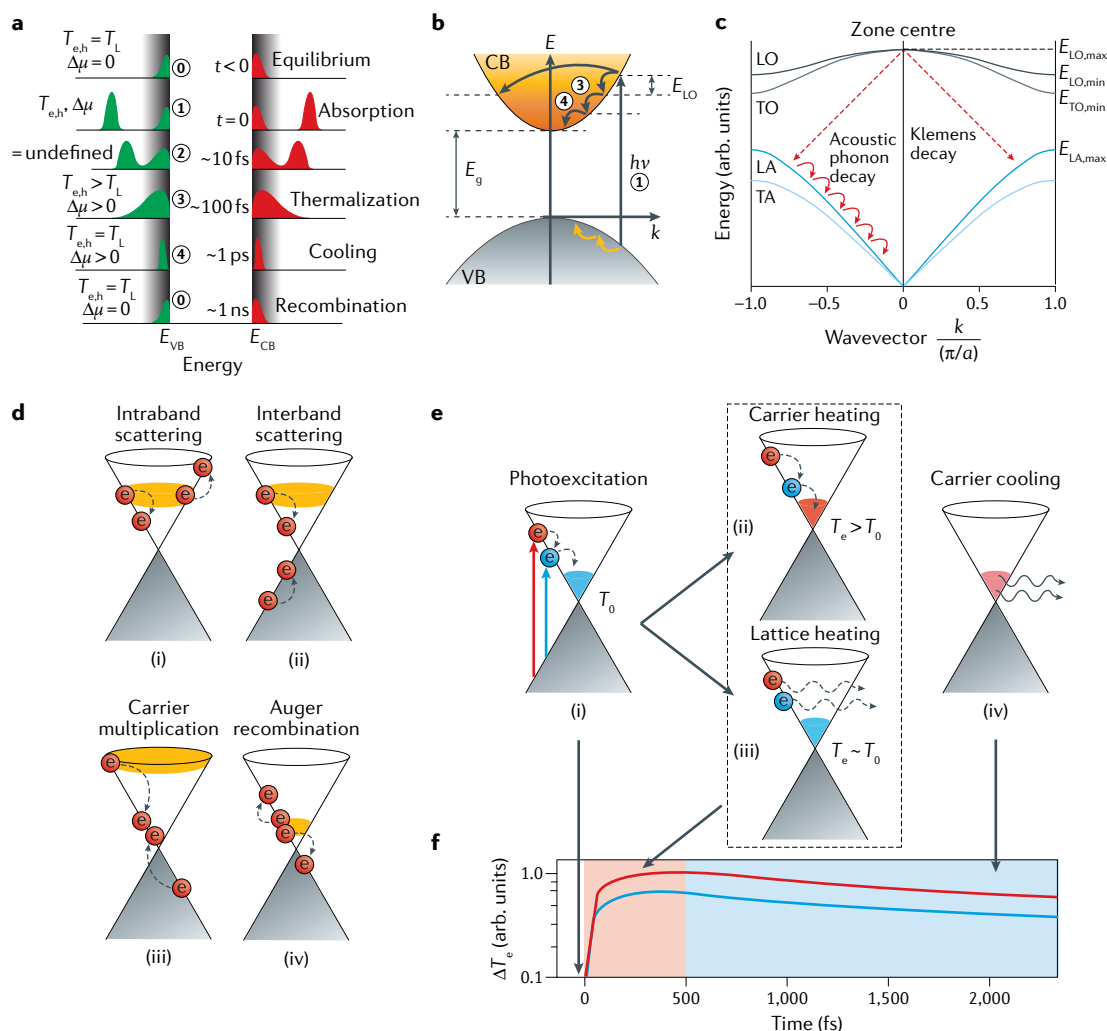
Fig. 2 | **Hot carrier dynamics in semiconductors and graphene. a** | Schematic illustration of the evolution of charge carrier distribution in the valence and conduction bands of a semiconductor with the delay time of pulsed laser excitation. At the thermal equilibrium state (step 0), charge carriers are at the same temperature as the lattice. After photoexcitation (step 1), ultrafast elastic carrier–carrier scattering transforms a nonequilibrium carrier distribution (step 2) to a thermal distribution of hot carriers in the conduction band (CB) and the valence band (VB) (step 3). Carrier cooling (step 4) forms in equilibrium with the lattice temperature prior to final recombination. $\Delta\mu$ represents the dynamic Fermi level splitting at various delay times. **b** | Schematic representation of photophysical processes leading to carrier cooling via longitudinal optical (LO) phonon (E_{LO}) emission in parabolic bands with different carrier effective masses. **c** | Phonon dispersion curve for a 3D diatomic material with predominant phonon decay paths in the zone centre, from higher-energy LO phonons to lower-energy acoustic phonons during heat dissipation[162]. TO, LA and TA stand for transverse optical, longitudinal acoustic and transverse acoustic phonon, respectively. **d** | Coulomb scattering in terms of intraband and interband scattering (processes i, ii). Auger processes can promote electron scattering from one band to another, leading to carrier multiplication or inverse Auger recombination (process iii) and Auger recombination[48] (process iv). **e** | Schematic representation of photon-assisted carrier dynamics in graphene with two different photon energies (red and blue arrows). Photoexcitation follows the carrier–carrier scattering and phonon emission, leading to carrier heating and lattice heating, respectively. **f** | Higher photon energy promotes efficiently heated electrons (hot electrons), generating larger photovoltage through the photo-thermoelectric effect (red curve) when compared with that of lower photon energy (blue curve)[105]. Shaded areas denote occupied states. Panels **a–c** adapted with permission from REF.[162], Royal Society of Chemistry. Panel **d** adapted from REF.[48], Springer Nature Limited. Panels **e** and **f** adapted from REF.[105], Springer Nature Limited.

(FIG. 2b, steps 3 and 4). This nonequilibrium population drives the reverse reaction by emitting the hot-phonon energy to reheat the carrier population, thus, increasing the carrier relaxation time. The nonequilibrium HC population leads to the dynamic splitting of the quasi-Fermi level, resulting in high open-circuit voltage[69]. Following the LO phonon emission, lattice anharmonicity allows

the further decay of LO phonons into acoustic phonons employing various mechanisms. The acoustic phonons possess higher thermal conductivity, leading to a superior heat dissipation. Consider a diatomic material for demonstrating phonon dispersion with degenerate optical and acoustic branches at the zone centre ($k = 0$), having maximum and minimum energy values,

respectively (FIG. 2c). The Klemens mechanism, also known as the principal decay mechanism, describes the decay of one optical phonon into two acoustic phonons with half its energy and equal but opposite momenta[70]. Additional decay processes include the Ridley mechanism and the Barman–Srivastava mechanism. The Ridley mechanism involves the decay of LO phonons from the zone centre into transverse optical and longitudinal acoustic phonons, which is usually responsible for the negligible energy loss to acoustic phonons compared with the Klemens decay[71]. Barman–Srivastava decay channels are active in hexagonal materials of wurtzite structure, in which each optical phonon decays into two optical phonons in a lower branch. However, this process is expected to have negligible impact at temperatures below 1,000 K.

Properties of HC absorbers

Based on the above considerations and various findings on slow HC cooling in different semiconductors with distinct dimensionalities, a variety of intrinsic material properties and engineering strategies can be enlisted to design an efficient HC absorber[72,73], such as the following.

First, a large phononic bandgap can suppress Klemens decay; the phononic bandgap ($E_{O, min} - E_{A, max}$) should be greater than the maximum value of the acoustic phonon energy ($E_{A, max}$). It is achieved in a material with large atomic mass difference[21]. Second, low LO phonon energy to reduce the energy lost per unit LO phonon emission; the energy of each LO phonon should be low. However, if the energy is too low, excessive LO modes can be generated, which also limits the HC energy with prolonged lifetime. Thus, each LO phonon is required to have optimal energy to give a suitable material for HC photovoltaics, but sufficiently high to avoid excessive assembly of LO modes. Third, low maximum acoustic phonon energy (E_A) to maximize the phononic bandgap, which can be achieved in a material with flat dispersion characteristics. Fourth, a narrow dispersion of optical phonon energy ($E_{LO, max} - E_{LO, min}$) to minimize the energy loss via Ridley decay, which can be achieved by choosing a material with crystal symmetry. Finally, a small electronic bandgap (<1 eV) to harvest a broad range of solar radiation.

HC absorbers with various dimensionalities

Semiconductor quantum dots have been extensively studied and explored for their application in HCSC absorbers because of their low-cost synthesis and tunable optical and electronic properties[74–76]. Apart from multiphonon emission, quantum dots possess various HC cooling pathways, including electron–hole energy transfer, carrier cooling or recombination associated with the surface states[77–80]. Thus, the presence of a phonon bottleneck is unlikely to be experimentally verified in bare quantum dots and is mostly observed in carefully engineered core–shell nanostructures[81,82]. Semiconductor quantum dots, however, possess high carrier confinement to increase Auger recombination (AR), which leads to a short relaxation time[78]. Additionally, quantum dots exhibit a narrowband optical absorption and, whereas

an ensemble of quantum dots may partially resolve the problem, it also introduces additional decay channels. Thus, quantum dots alone are not a suitable candidate for an efficient HCSC absorber.

HC dynamics in graphene

In addition to specially engineered semiconductors, graphene has emerged as an alternative, promising system to explore solar energy harvesting via the redistribution of HC energy. An atomically thin graphene layer absorbs ~2.3% of incident light with uniform spectral response, because of its unique linear band structure[83,84]. Predominant carrier scattering via optical phonons results in a significant number of photoexcited HCs in graphene. Furthermore, the hot optical phonon bottleneck effect in graphene delays the thermalization of HCs particularly near the Dirac point, because of the velocity mismatch and momentum conservation that restrict direct carrier–acoustic phonon interactions[85]. After initial cooling, the low-temperature cooling channel becomes predominant and transfers energy to the acoustic phonons[86]. Therefore, formation of the acoustic phonon bottleneck effect may also be an important parameter for HC-driven photovoltaics. Additionally, graphene possesses a high carrier velocity of ~10^6 m s^{-1}, resulting in a large scattering volume (or area for 2D materials), which leads to a long mean free path of HCs (up to ~1 μm)[48,87–90].

Two-body scattering

Coulomb-mediated two-body scattering in monolayer graphene is schematically shown in FIG. 2d. The linear dispersion at the K-point in graphene allows interband carrier–carrier scattering, owing to the simultaneous energy and momentum conservation[91]. This physical phenomenon is governed by Auger processes, in which one of the two involved HCs (either two electrons or two holes) offers bridging between the valence band and the conduction band, whereas the other charge carrier remains in the same band (FIG. 2d). Therefore, Auger scattering alters the overall carrier density in the respective bands and are distinguished as CM (inverse AR) and AR. In CM, a hot electron scatters against a valence band electron, leading to its ejection from the Fermi sea to the unoccupied conduction band and generating two hot electrons. In AR, two hot electrons in the conduction band scatter with each other, leading to the generation of a hot electron with higher energy and an electron in the valence band with lower energy[48,92]. When a graphene sheet is optically excited, a dynamic competition is observed between CM and AR processes, leading to the rapid thermalization of HCs within a few tens of fs (REFS[93–95]). HCs further equilibrate with optical phonons within ~1 ps, followed by cooling via acoustic phonon emission, which extends up to ~100 ps. The electronic temperature of HCs in graphene can reach as high as 1,000 K and be sustained over a long time (ps), which is attributed to the low heat capacity of electrons and the vanishing density of states near the Dirac point[91,96]. A recent theory predicts that disorder in graphene relaxes the momentum conservation constraint, leading to the emission of acoustic phonons with

---

Auger recombination

(AR). Interband carrier–carrier scattering reducing the overall carrier density in the conduction band.

large energy and momentum. This mechanism is called disorder-assisted scattering or supercollision cooling, having orders of magnitude faster relaxation time than the disorder-free model[97]. This theoretical prediction of faster hot electron cooling near the Fermi level was later quantitatively verified experimentally[98].

HC dynamics and extraction

Photovoltage generation by the photo-thermoelectric (PTE) effect is typically driven by the HCs in graphene[99–101]. This phenomenon is observed with a focused optical irradiation at the interface of monolayer and bilayer graphene or at the interface of two layers of graphene with different Fermi energies, E_F (REFS[99,100,102–104]). The PTE voltage, V_{PTE}, of a graphene device directly depends on the absorbed-light-induced local heating of electrons and the Seebeck coefficient difference — that is, $V_{PTE} = (S_2 - S_1)(T_e - T_0)$, where S_1 and S_2 represent the Seebeck coefficients at different regions, and T_0 and T_e are the temperatures of electrode heat sinks and hot electrons, respectively[105]. The switching speed and timescale of photovoltage generation in a PTE device are determined by the dynamics of photogenerated charge carriers. As schematically depicted in FIG. 2e,f, following photoexcitation, electrons are ejected from the Fermi sea to the unoccupied conduction band states (process i), successively leading to electron–electron scattering (process ii) and then electron–phonon scattering (process iii), which respectively heat up the electrons and the lattice within a few fs. Finally, hot electrons reach a thermal equilibrium with the lattice by dissipating their energy via acoustic phonon emission on a ps timescale (process iv). As electron heating attributes to the generation of photovoltage, electron heating dynamics and intrinsic carrier heating efficiency can determine a PTE device's performance. Ideally, the absorption of higher-energy photons corresponds to a higher electron temperature, leading to a greater photovoltage (FIG. 2f). In contrast, the switching speed of a graphene-based device is determined by the carrier cooling time, which is limited to the ~ps scale.

Despite the aforementioned potentials, the implementation of graphene as a HC absorber in practical solar cells is still a challenge. Large-scale synthesis of defect-free graphene is a recent development[106]. Additionally, the integration of monolayer graphene with a conventional bulk electron acceptor (TiO$_2$, ZnO, etc.) is limited by a momentum barrier. Hot electrons in graphene are generated near the K-point, whereas the conduction band minima of common electron acceptors are at the Γ-point. Thus, the momentum barrier prevents an efficient hot electron transfer from graphene to the electron acceptor surface. This momentum mismatch can only be compensated by phonon emission that reduces the energy of HCs, resulting in a low V_{OC} and PCE.

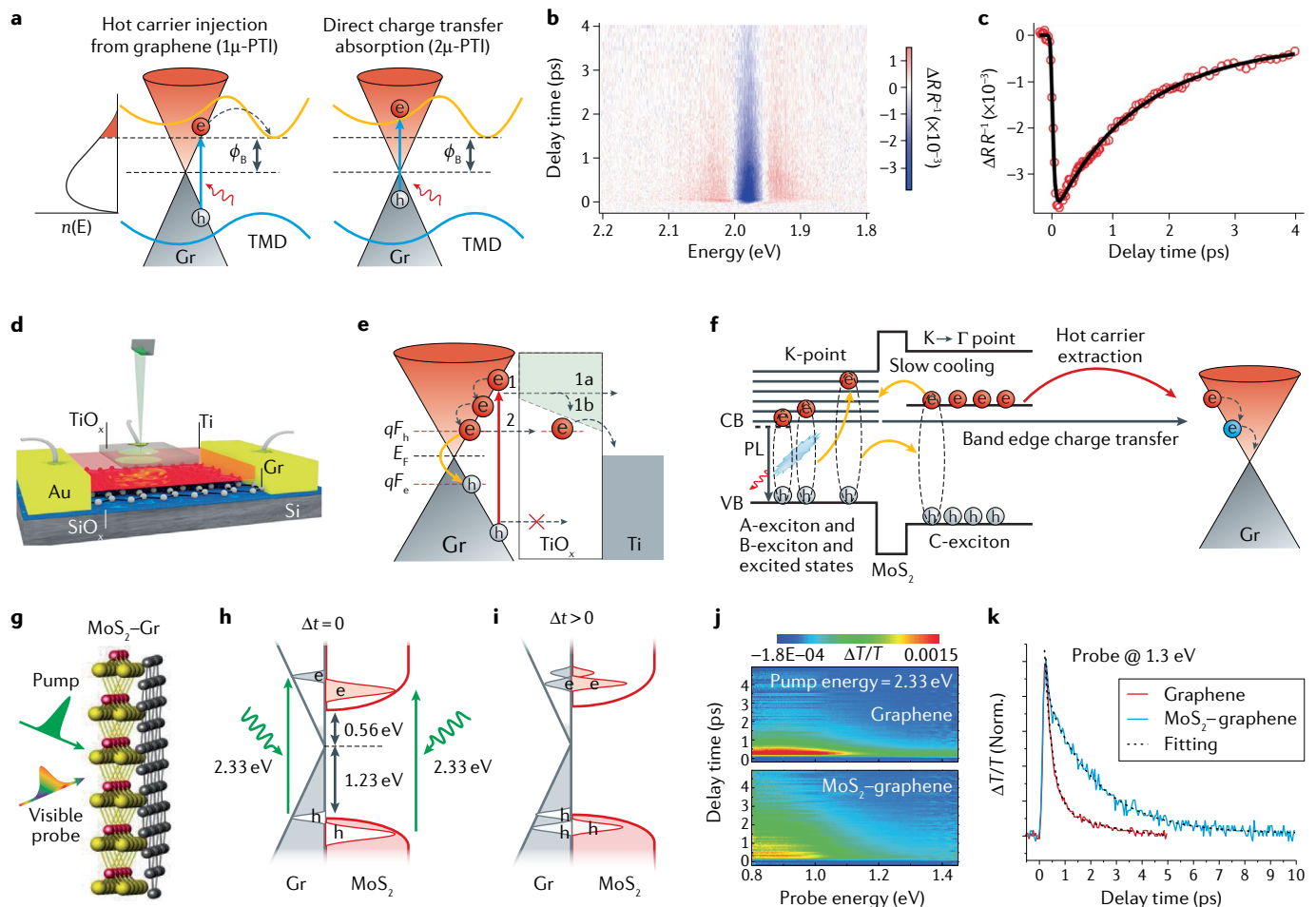### HC extraction in graphene–semiconductors

The above-mentioned problems may be partially overcome by relaxing the momentum requirement for an efficient interfacial charge transfer, which can be achieved by the choice of spatially confined nanomaterials, such as graphene quantum dots or nanoribbons[107].

Another promising approach for an efficient interfacial HC transfer is to integrate the graphene nanosheet with a semiconductor material with vanishing momentum mismatch. Monolayer TMDs possess conduction band minima near the K-point and can be a promising class of hot electron emitters or collectors in a solar cell upon graphene integration[108]. In addition, thin hexagonal boron nitride (hBN) also has a valence band maximum and conduction band minimum near the K-point and can act as both an electron acceptor and an electron emitter. Although it has a large bandgap energy, a direct interlayer HC transfer possibly occurs due to the momentum matching at the K-point, for example, from a vdW material (graphene or semiconducting TMD) to hBN[109]. In such a case, hBN can act as a hot electron acceptor. hBN can also accept hot electrons through thermionic emission in the graphene–hBN heterostructure[110]. Furthermore, optical excitation in defects of hBN may excite electrons in its conduction band, following the electron transfer to graphene and, thus, hBN acts here as an electron emitter[111]. However, the issues arising from the large bandgap requires further investigation. Furthermore, weak light absorption and ultrafast relaxation time of a few ps of HCs in graphene hinder the efficient electron–hole pair generation and HC extraction, limiting its implementation for HC-based energy harvesting. As the HC relaxation time is directly proportional to the photogenerated carrier density in graphene, an increase in optical absorption and the consequent delay in HC cooling may be one of the key factors for designing a graphene-based HC device for energy harvesting[60,112]. The weak absorption of graphene could be compensated by integrating the graphene layer with 2D vdW layered semiconductors that yield relatively high absorbance, leading to the synergistic performance[113].

Graphene as a HC injector

Hot electron injection from graphene to TMDs can be categorized into two distinct pathways. First, rapidly thermalized hot electrons with prolonged lifetimes (>1 ps) exhibit a long tail in the higher-energy domain, a part of which may surpass the Schottky barrier (Φ_B). These hot electrons with excess energy can transfer into the TMD through photo-thermionic (PTI) emission, referred to as the conventional PTI (1μ-PTI) pathway; this is usually observed in multilayer TMDs[91] (FIG. 3a). However, a substantial amount of energy is lost during the carrier thermalization and the subsequent interlayer migration, thereby, resulting in low internal quantum efficiency of ~2%. It is possible, though challenging, to enhance this up to ~20% by tuning the hot electron temperature (~1,000 K) and Schottky barrier height (~0.06 eV)[90,114,115]. Next, owing to the momentum conservation, photocarrier generation after sub-bandgap excitation by direct absorption of interlayer charge transfer from graphene to atomically thin TMDs is referred to as the 2μ-PTI pathway[61] (FIG. 3a). The injection quantum yield (internal quantum efficiency) of photogenerated HCs in an atomically thin graphene–WS$_2$ heterostructure is reported to be as high as ~55% with 1.6-eV photoexcitation[91].

Internal quantum efficiency
Ratio between the number of photocarriers collected and the number of photons absorbed by the graphene layer.

Fig. 3 | **Hot carrier extraction in the graphene–semiconductor heterointerface. a** | Simplified band diagram illustrating photocarrier generation via the conventional photo-thermionic effect and direct absorption of charge transfer transition at the graphene–WS$_2$ interface with sub-bandgap photoexcitation. Graphene allows ultrafast thermalization of photoexcited carriers generating the hot electron distribution $n(E)$ shown in the tail (red shaded area), for surpassing the Schottky barrier, Φ_B, and generating a thermionic current[115]. **b** | Energy-resolved transient reflectance spectra of the graphene–WS$_2$ heterostructure, excited by a sub-bandgap photoexcitation of 1.6 eV and showing an exciton bleach signal of WS$_2$. **c** | Time-resolved differential reflection of the graphene–WS$_2$ heterostructure with a long decay time (~1.2 ps), indicating a hot electron transfer from graphene to the WS$_2$ layer[91]. **d** | Schematic illustration of a Gr–TiO$_x$–Ti device demonstrated for hot carrier (HC) extraction from graphene. **e** | Electronic band diagram of a Gr–TiO$_x$–Ti heterostructure. Here, $qF_{h(e)}$ denotes the quasi-Fermi level of holes (electrons). Primary HC extraction mechanisms are shown by horizontal dashed arrows 1 and 2 (REF.[118]). Step 1a (step 1b) indicates charge transport through the empty conduction band (defect states) in the TiO$_x$ layer. Step 2 indicates the tunnelling of HCs from the quasi-Fermi level in graphene to the Ti electrode (Poole–Frenkel tunnelling). **f** | Schematic representation of various photophysical processes in monolayer MoS$_2$ and initial electron extraction by graphene in the MoS$_2$–graphene interface[63]. **g** | Schematic illustration of the MoS$_2$–graphene heterostructure for transient differential transmittance spectra. Schematic illustration of the initial population before interlayer charge transfer ($\Delta t = 0$) (panel **h**) and HC distribution after the interlayer charge transfer ($\Delta t > 0$) (panel **i**). Filled and empty colour schemes represent the electrons and the holes, respectively. Green arrows represent the initial pump–photon energy of 2.33 eV. **j** | Differential transmittance map as a function of pump–probe delay time and probe energy for bare graphene (top panel) and the MoS$_2$–graphene heterostructure (bottom panel) with a pump–photon energy of 2.33 eV. **k** | Transient absorption dynamics for bare graphene and heterostructure at a probe energy of 1.3 eV. CB, conduction band; PL, photoluminescence; PTI, photo-thermionic; TMD, transition metal dichalcogenide; VB, valence band. Panel **a** adapted with permission from REF.[61], AAAS, and REF.[115], CC BY 4.0 (https://creativecommons.org/licences/by/4.0/). Panels **b** and **c** adapted with permission from REF.[91], AAAS. Panels **d** and **e** adapted with permission from REF.[118], ACS. Panel **f** adapted from REF.[63], CC BY 4.0 (https://creativecommons.org/licences/by/4.0/). Panels **g**–**k** adapted with permission from REF.[60], ACS.

The two above-mentioned processes have been verified experimentally via ultrafast transient absorption and/or reflection spectroscopy and/or microscopy techniques considering pump-photon energies below the TMD bandgap, thereby, ensuring the excitation of only graphene and an interlayer charge transfer[61,91]. Photocurrent generation in TMDs by hot electron transfer from graphene via the 1μ-PTI pathway is slow (~47 ps)[91], whereas it is extremely fast via the 2μ-PTI

pathway and is mostly limited by the experimental time resolution[116,117]. A dominant bleach peak owing to the specific resonant interband transitions is observed in the colour plot of transient reflection spectra for an atomically thin graphene–WS$_2$ structure at ~1.98 eV (FIG. 3b), which can be attributed to the A-exciton peak of WS$_2$ from its bandgap renormalization. The corresponding fitted kinetics (FIG. 3c) yield an ultrafast rising time (~27 fs) and prolonged biexponential decay (half-life

of ~1.2 ps), which corresponds to a direct hot electron excitation from graphene to the WS_2 layer following the transition of electrons back to graphene[91]. It is reported that HCs and their energies are mostly confined and conserved in the early stages of intraband scattering processes[48,90,114], and an ideal strategy to harvest such energies is to efficiently collect the quasi-thermalized HCs. As the photocarrier generation time in the 2µ-PTI pathway is comparable to the intraband electron–electron scattering time in graphene, this process may be considered as a prerequisite for efficient HC energy harvesting in a solar cell.

Extraction of HCs. The proof of concept for extraction of HCs from graphene-based 2D photovoltaic device was first demonstrated with a graphene–TiO_x–Ti heterostructure (FIG. 3d) with maximum V_{OC} and I_{SC} of 0.3 V and 14 nA, respectively[118]. Two distinct mechanisms possibly responsible for HC extraction from graphene to a Ti electrode via a TiO_x layer are discussed in detail (FIG. 3e). In the first mechanism, the optically excited electrons in graphene with an energy higher than the conduction band minima of the TiO_x layer can be transferred directly to the Ti electrode before relaxation within the graphene or recombination in the TiO_x layer. Charge transport in this process mainly occurs through the conduction band (step 1a) or defect states (step 1b) in the TiO_x layer (F^+ and Ti^{3+} centre)[119–121]. In the second mechanism, the photogenerated hot electrons undergo ultrafast thermalization to the quasi-Fermi level in graphene with a much longer lifetime because of the formation of a phonon bottleneck, followed by a tunnelling to the Ti electrode either directly or through the defect levels in the TiO_x layer (Poole–Frenkel tunnelling). Additionally, an efficient carrier–carrier scattering in graphene may lead to the generation of secondary hot electrons in the conduction band (CM process), thereby, contributing to the photocurrent[122]. Moreover, the deep-lying valence band edge of the TiO_x layer restricts the migration of photoexcited holes from graphene to the Ti electrode, making the architecture unique and advantageous for photovoltaic performance.

Graphene as a HC acceptor

In addition to the excellent HC injector characteristics, graphene has proven its suitability as an efficient HC collector in atomically thin graphene–TMD heterostructures[63,117]. Compared with pristine monolayer MoS_2, the initial carrier extraction efficiency from MoS_2 to graphene was calculated to be 93%, 81% and 80% for the A-exciton, B-exciton and C-exciton states, respectively[63]. The carrier extraction efficiency from the C-exciton band (so far only seen in MoS_2–graphene structures) is attributed to a prolonged HC relaxation (~350 ps), which is at least three orders of magnitude slower than that for parallel bands in the density of states in twisted bilayer graphene (~0.2 ps). An illustration explaining the detailed photophysical processes for efficient HC transfer via the C-exciton band is shown in FIG. 3f. Moreover, a recent report has demonstrated an ultrafast selective interlayer charge (hole) transfer from monolayer WS_2 to graphene, which attributes

to the higher number of available final states for hole transfer[123]. In addition to the interlayer carrier transfer, an atomically thin graphene-based 2D heterostructure ($MoSe_2$–graphene) effectively transfers energy from $MoSe_2$ to graphene via Dexter-type and Förster-type energy transfer processes[124].

Recently, a method of enhancing the HC effect in graphene was demonstrated by employing efficient interfacial photogenerated HC transfer in the MoS_2–graphene heterostructure (FIG. 3g) with a prolonged relaxation time by broadband transient differential transmittance (TDT) spectroscopy[60]. The Dirac point of graphene is near the conduction band edge of MoS_2, which allows the incident photons to populate the photoexcited carriers in graphene at higher energies (0.67 eV) than those of MoS_2 (FIG. 3h). First-principles calculations suggest that interlayer charge transfer through the heterointerface takes place nondissipatively via electronic interaction, leading to a two-peak band structure (FIG. 3i) of HCs, which is supported by experiments. To investigate the effect of interlayer HC transfer on carrier dynamics in graphene, TDT mappings were acquired with near-infrared broadband probe energy (0.8–1.5 eV) and pump–probe delay time for bare graphene and the MoS_2–graphene heterostructure (FIG. 3j). The carrier relaxation time of graphene in the heterostructure is prolonged by four times compared with that of bare graphene monitored at different probe energies (FIG. 3k). The estimated hot electron temperature of graphene in the heterostructure is ~3,000 K at earlier delay time (<1 ps), which sustains for a long delay time and remains hotter than that of bare graphene. This is attributed to the strong electron–phonon interaction, originating from the large population of photoexcited carriers in graphene after the efficient interfacial charge transfer from MoS_2. Thus, the prolonged relaxation time in graphene of the MoS_2–graphene heterostructure verifies the hot-phonon bottleneck effect. The nondissipative interlayer photogenerated charge transfer is further evidenced by significantly reduced peak amplitude as, well as the relaxation time of A-excitons and B-excitons of MoS_2 in the heterostructure in visible TDT spectra. Therefore, graphene-based 2D vdW heterostructures with superior light absorbance capability can be a promising candidate for efficient extraction of HCs and its realization in practical HCSCs.

Photovoltaics in atomically thin p–n junctions

High-quality heterointerfaces in vdW semiconductors with nearly free dangling bonds reveal a new class of versatile devices with various advantages over conventional covalently bonded defective materials[125]. An atomically thin vdW layered p–n heterojunction demonstrating a rectifying optoelectronic and photovoltaic response was first realized in a monolayer WSe_2 (p-type) and MoS_2 (n-type) semiconductor heterostructure[126] (FIG. 4a, lateral view; FIG. 4b, vertical view). The p–n heterojunction exhibits gate-tunable photovoltaic characteristics under white light illumination (FIG. 4c). Even after the dissociation of optically excited charge carriers in the p–n heterojunction, interlayer recombination through inelastic tunnelling via Shockley–Read–Hall

---

A-exciton, B-exciton and C-exciton states
A and B excitonic states arise due to spin–orbit-coupling-induced valence band splitting at the K-point. The C-exciton originates from the band nesting region on the higher-energy side.
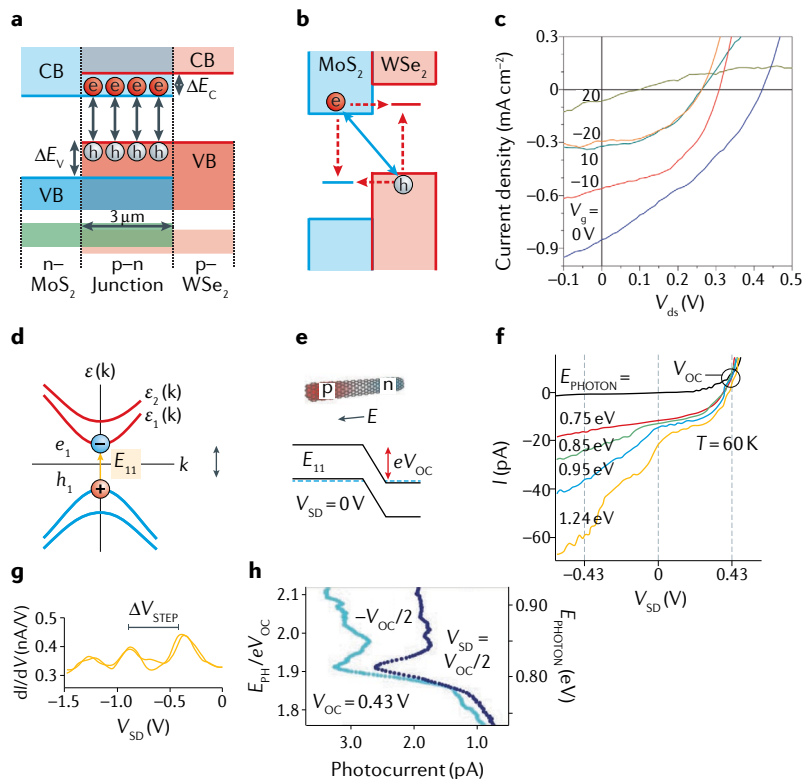
Fig. 4 | **Gate-tunable photovoltaic characteristics of an atomically thin p–n junction.**
a,b | Band alignment of an atomically thin WSe$_2$–MoS$_2$ heterojunction in the lateral and vertical directions, respectively. ΔE_C and ΔE_V respectively represent band offset for electrons and holes across the interface. Interlayer recombination via Shockley–Read–Hall (black arrows in panel **a** and red arrows in panel **b**) or Langevin (blue arrow in panel **b**) mechanisms drives the dark current. **c** | Photovoltaic response under white light at various gate biases[126]. **d–h** | Carrier-multiplication-induced photocurrent characteristics, step interval ΔV_{STEP} of photocurrent and its temperature dependence in single-walled carbon nanotube (SWCNT) p–n junction photodiodes. **d** | Schematic representation of electronic band structure of a SWCNT showing the photoexcited electron–hole pair in the first subband ε_1. **e** | SWCNT showing p-type and n-type regions with built-in electric field E (top). Potential energy diagram with respect to the length of the nanotube p–n junction at $V_{SD} = 0$ V (bottom). The Fermi level is denoted by the dotted lines, whereas E_{11} is the bandgap energy. **f** | I–V_{SD} characteristics for a SWCNT p–n junction device with various photon energies at $T = 60$ K with nanotube diameter $d = 1.4$ nm, optical power density 25 W cm^{-2}, $V_1 = -V_2 = 7.5$ V and $V_G = 1.2$ V. **g** | Reverse bias differential conductance $|dI/dV_{SD}|$. **h** | Photocurrent spectra for the device in panel **f** at optical power density = 3 W cm^{-2}. Left axis normalized by eV_{OC} (REF.[49]). CB, conduction band; VB, valence band. Panels **a–c** adapted from REF.[126], Springer Nature Limited. Panels **d–h** adapted with permission from REF.[49], AAAS.

(FIG. 4a, black arrows; FIG. 4b, red arrows) or Langevin (FIG. 4b, blue arrow) mechanisms may play an important role in determining the photocurrent (I_{SC}), which can be tuned by the gate voltage[127].

CM in a p–n homojunction

The signature of the CM-assisted enhanced photocurrent generation in vdW materials was first demonstrated by a single-walled carbon nanotube (SWCNT) p–n homojunction photodiode[49]. Generation of multiple electron–hole pairs from a single HC was demonstrated through spatially and spectrally resolved photocurrent, showing distinct photocurrent steps at voltage intervals equivalent to the bandgap energy (E_{GAP}/e). SWCNTs generate an electron–hole pair when excited
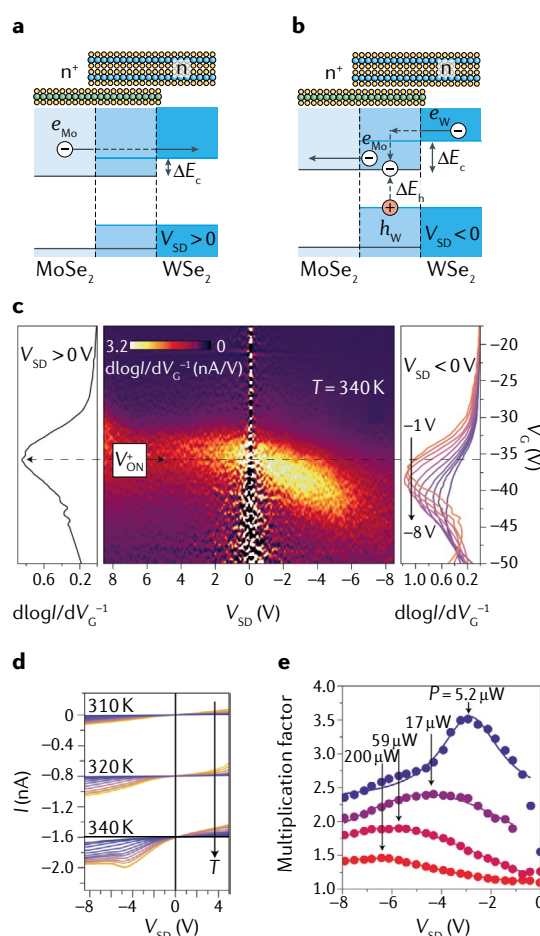
to the first subband ε_1 with bandgap energy E_{11}, whereas higher-energy photons may promote the excitons with a heavier effective mass to the higher-energy subband ($E_{22} = 2E_{11}$) (FIG. 4d). The p–n homojunction is realized by inducing selective electrostatic doping along the nanotube length (FIG. 4e). Thus, the built-in electric field, E, promotes the separation of the photogenerated charge carriers at the junction and the collection of these carriers by the device contacts, leading to the photovoltaic behaviour. Under dark and low-energy photon ($E_{PHOTON} < 2E_{GAP}$) illumination, the I–V_{SD} characteristics follow a regular p–n junction transport behaviour with a threshold turn-on voltage ($V_{OC} = 0.43$ V), which corresponds to the bandgap energy ($E_{GAP} = E_{11} \sim eV_{OC}$) of the carbon nanotube. The reserve bias photocurrent measured at low temperature (60 K) increases with photon energy and consists of a series of photocurrent steps with an increasing reverse bias (FIG. 4f). The photocurrent steps strongly depend on source-drain bias, temperature and incident photon energy. Differential conductance, $|dI/dV_{SD}|$, plotted as a function of V_{SD} (FIG. 4g) shows more precise steps and is close to the E_{GAP} value ($\Delta V_{STEP} \approx E_{GAP} \approx 0.4$ eV). Additionally, photocurrent spectra exhibit photocurrent steps when excited with a photon energy $E_{PHOTON} > 2E_{11}$, indicating a carrier excitation to the second subband (ε_2) with a distinct spectral peak near $E_{PHOTON} = 2E_{11}$ (FIG. 4h). The photocurrent steps are attributed to the generation of high-energy carriers in the second subband, following the integration of their excess rest mass energy with the kinetic energy of the electric field, which leads to the generation of an electron in the first subband, e_1, along with additional electron–hole pairs ($e_2 + E_k(x) \rightarrow e_1 + n(e_1 + h_1)$), often referred to as impact excitation (CM). The integer $n = 1, 2, 3\ldots$ indicates the number of electron–hole pairs in the final state and $E_k(x)$ indicates the kinetic energy available to the electrons generated at position x along the p–n junction. Furthermore, the photocurrent steps are observed only at temperatures below 90 K. Above 90 K, HC relaxation via optical phonon emission is highly efficient; additionally, the radial breathing mode of the SWCNT is activated, leading to a negligible impact excitation. Later experiments on nanotubes using ultrafast transient absorption spectroscopy found CM (quantum yield ~130%) at room temperature when $E_{PHOTON} \approx 3E_{GAP}$ (REF.[128]). While the first quantification of photocurrent in a carbon nanotube photodiode by optoelectronic measurement was found to be ~3%[129], the enhanced photocurrent quantum yield (~30%) was later achieved in a suspended nanotube p–n junction with $E_{PHOTON} > 4E_{GAP}$ (REF.[130]). Large axial electric-field-driven CM was further demonstrated to have high photocurrent quantum yield (>100%) in these suspended nanotube p–n junction photodiodes[131]. This is substantial advancement towards realizing an ultra-efficient photovoltaic device technology, beyond the SQ limit.

Interlayer CM

Following previous reports, highly efficient interlayer CM from an impact excitation of hot electrons in a 2D vdW heterostructure photocell was demonstrated near room temperature (≥340 K)[132]. An atomically thin

WSe$_2$–MoSe$_2$ heterojunction-based near-infrared photodetector was studied, exhibiting 350% enhancement in responsivity resulting from the interlayer CM (FIG. 5). The energy of excited carriers in the WSe$_2$ layer with minimum excess energy is an aggregate of the interlayer potential energy (ΔE_C) and kinetic energy of the electric field, which leads to the generation of a low-energy electron in MoSe$_2$, along with an interlayer electron–hole pair ($e_{WSe_2} + K_e(V_{SD}) \rightarrow e_{MoSe_2} + (e_{MoSe_2} + h_{WSe_2})$). With an increasing reverse bias, the potential energy of e_{WSe_2} increases, whereas the interlayer bandgap energy (ΔE_h) decreases, leading to higher interlayer recombination. The gate-voltage-dependent interlayer current was examined to verify the unaffected V_{ON} (threshold gate voltage, V_G, beyond which interlayer electron transfer starts) in forward bias ($V_{SD} > 0\,V$) and the lower

V_{ON} in reverse bias ($V_{SD} < 0\,V$) (FIG. 5a–c). At $V_{SD} > 0\,V$, the colour map exhibits a peak near $V_G = -36\,V$, which does not change in the forward bias (FIG. 5c). In contrast, V_{ON} decreases linearly with an increasing reverse bias, which may be attributed to the generation of additional electrons in the MoSe$_2$ conduction band; this increases the electron density in the interlayer channel, which reduces V_{ON} (FIG. 5c). A reverse bias photocurrent attributed to the CM, which increases with temperature, is fully consistent with the impact excitation for dark current. The WSe$_2$–MoSe$_2$ n$^+$–n heterojunction exhibits non-monotonic I–V_{SD} characteristics in reverse bias with an increasing temperature[133]. The reverse bias current at high V_G shows a prominent peak when the temperature reaches a threshold value ($T = 340\,K$) (FIG. 5d). In contrast to the expected temperature-independent forward bias current, the reverse bias interlayer current ($I \propto T^2 \exp(-1/T)$) increases with temperature at a low bias voltage and leads to a peak at higher temperatures, which can be attributed to the interlayer electron–hole multiplication. Additionally, interlayer recombination increases with V_G, as it promotes more electrons to recombine with the holes created via impact excitation. Thus, the current increment through CM competes with the interlayer recombination, resulting in a negative differential conductance and a dark current peak arising (FIG. 5d). As the CM is suppressed at low temperature, the multiplication factor is quantified by calculating the responsivity ratio, R_{350K}/R_{300K} (FIG. 5e). The enhancement factor at low optical power exceeds 3.5, showing a distinct peak at $V_{SD} = -2.8\,V$, which closely matches the maximum differential conductance because of a dark CM. The enhancement factor is reduced with the excitation of high-power photons, probably resulting from an efficient electron–hole annihilation and thermal effects. Therefore, atomically thin, ultra-efficient optoelectronic and photovoltaic devices driven by HC and CM effects may be realized near room temperature.

Interlayer HC generation

Ultrafast formation of interlayer HCs, which drives CM in vdW heterojunctions, was demonstrated in a MoS$_2$–WS$_2$ heterostructure by energy-state-resolved ultrafast microspectroscopy[42]. Despite the apparent momentum mismatch between the intralayer (or interlayer) excitons and high Coulomb barrier in 2D geometry, interlayer charge transfer is adequately efficient and observed to be nearly independent of the aforementioned parameters, which leads to the generation of a high photocurrent in ultrathin photovoltaic devices. Upon preferred optical excitation, electrons can be excited to both the excitonic band as well as the conduction band, leading to the formation of tightly bound excitons and weakly bound electron–hole pairs, respectively, following the fast interlayer charge transfer (~0.8 ps)[42]. Fast decay dynamics imply that the tightly bound interlayer excitons cannot be created immediately after the interlayer charge transfer. Instead, the carrier transfer follows an intermediate electron–hole pair generation with excess energy and is termed as hot excitons (FIG. 6). The excess energy of the intermediate hot excitons allows the sampling of the momentum space

Fig. 5 | **Hot-carrier-driven interlayer current and carrier multiplication in a 2D semiconductor heterojunction photocell. a,b** | Electronic band profiles for a MoSe$_2$–WSe$_2$ heterojunction in forward bias ($V_{SD} > 0\,V$) and reverse bias ($V_{SD} < 0\,V$), respectively. **c** | Colour map of interlayer current (dlog$I$/dV_G) as a function of gate voltage (V_G) and source-drain voltage (V_{SD}). **d** | Interlayer I–V_{SD} characteristics at various temperatures ($T = 310$, 320 and 340 K) and V_G increasing from −50 V to 10 V (dark purple to orange). **e** | Multiplication factor of interlayer carriers estimated at various optical power fluences. Solid lines represent the Lorentzian fit[132]. Adapted with permission from REF.[132], Springer Nature Limited.
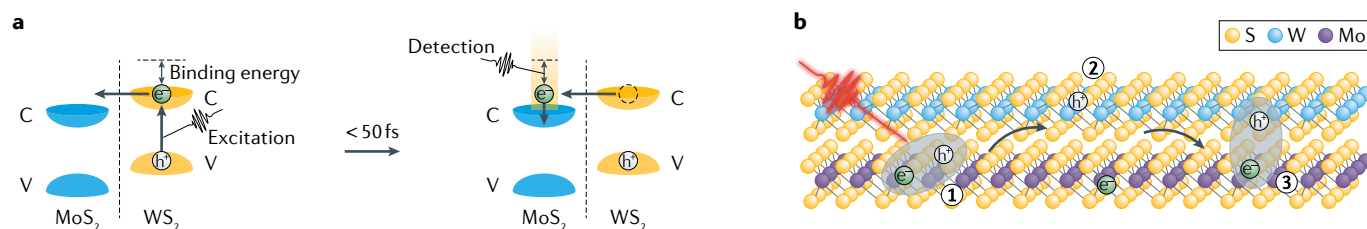
Fig. 6 | **Light-induced charge separation and ultrafast formation of interlayer hot excitons. a** | Charge separation processes and ultrafast formation of interlayer hot excitons in a MoS_2–WS_2 heterostructure. **b** | Schematic illustration of light-induced carrier separation and generation of interlayer hot carriers[42]. Panels adapted from REF.[42], CC BY 4.0 (https://creativecommons.org/licences/by/4.0/).

across a broad range, thereby, overcoming the momentum conservation requirement. Moreover, a hot exciton leads to the formation of electron–hole pairs with lower binding energy, which are dissociated (utilizing the excess energy) at a larger distance than that of the interlayer excitons. Consequently, the intermediate HCs may easily be extracted before cooling to tightly bound interlayer excitons, thereby, contributing to an enhanced photovoltaic performance.

From the above discussions, we conclude that the vdW heterostructures are a unique combination of two vdW materials with momentum conservation at the K-point, ensuring the efficient HC transfer through the interface without phonon decay. In an appropriate vdW heterostructure, ultrafast formation of interlayer HCs as well as interlayer CM can be achieved. The HC cooling dynamics of graphene is greatly influenced by the other TMD materials when it is integrated in a graphene–vdW TMDs heterostructure. TMD materials with higher solar absorbance change the photogenerated carrier density in graphene. Thus, prolonged HC cooling is achieved in graphene simply by the formation of vdW heterostructures. The above-mentioned advantages of vdW heterostructures may lead to the new design of high-performance HCSCs.

In contrast to quantum dots and 2D vdW heterostructures, multiple quantum well structures offer a continuous carrier density of states, resulting in a broadband solar energy absorption. Moreover, this unique structure opens up a phononic bandgap, thereby, reducing the carrier relaxation. Several reports have demonstrated the slow HC cooling in various compound semiconductors, such as InGaAs, GaAs–AlGaAs and GaAsP–InGaAs quantum well heterostructures[134,135]. A practical HC device has been demonstrated with enhanced current and voltage ($V_{OC} \approx 0.9\,V$)[136,137], achieving a PCE of 11.6% in a single InGaAsP quantum well solar cell[135]. The HC 'valley photovoltaic' effect has been recently reported in the InGaAs–AlInAs quantum well heterostructure and demonstrated high HC photovoltaic performance (short-circuit current density, $J_{SC} = 22\,mA\,cm^{-2}$ and $V_{OC} = 1.25\,V$)[138].

The vdW heterostructures, a promising class of materials for efficient HC photovoltaics, is a recent discovery. Thus, studies reported so far mostly use the ultrafast transient spectroscopic techniques. A few reports on vdW p–n heterojunctions demonstrate a considerably high photovoltaic effect ($V_{OC} \approx 0.5\,V$ for MoS_2–WSe_2; $V_{OC} \approx 0.64\,V$ and $J_{SC} \approx 6.5 \times 10^3\,mA\,cm^{-2}$

for ReS_2–$WSe_2)$[126,139]. Although the vdW heterostructures possess reasonably high photovoltaic performance, a detailed study of HC effects is missing and it still remains within the micro-scale devices. Thus, we believe that further investigation and development are necessary on the vdW heterostructures for proper comparison with the well-established quantum well superlattice structures.

HC effects in perovskites

Perovskites have emerged as one of the most promising solar cell absorber materials, with several advantages, including strong hot-phonon bottleneck effect in the presence of a nonequilibrium LO phonon population, leading to slow HC cooling, which is a key material criterion for the development of an efficient HCSC[18,140,141]. The HC cooling mechanism in 3D organic halide perovskite is mainly associated with the interplay of electron–LO phonon scattering with LO phonon decay, depending on the initial carrier density and pump-photon energy[141] (FIG. 7a). An interplay of hot phonons with Auger heating effects further retard the HC cooling at high carrier concentrations. A strong phonon bottleneck effect is observed in hybrid perovskites with ~10 times slower carrier–phonon relaxation rate compared with the inorganic counterpart, which is responsible for the upconversion of low-energy acoustic phonons into LO phonons[142]. The temperature-dependent interplay of emitted LO-phonon-mediated cooling with polaron formation has a dominant influence on the HC cooling rate in organic and inorganic perovskite nanocrystals[143–145]. At high temperature, the retarded HC cooling in $CsPbBr_3$ nanocrystals is reported to be solely responsible for the polaron formation, whereas the absence of polaron formation at low temperature leads to rapid cooling[145]. Femtosecond rise in the photoconductivity observed in organic and inorganic single-cation lead-iodide perovskite nanocrystals can be well described quantitatively using a simple model of sequential charge carrier cooling and polaron formation[144]. The HC temperature of organic halide perovskite nanocrystals is higher than its bulk counterparts and conventional semiconductor nanocrystals under a comparable photoexcitation (FIG. 7b). Slow HC cooling in perovskite nanocrystals has demonstrated CM with quantum yield up to 98%[56]. Therefore, synergistic HC photovoltaic effects could be expected in vdW heterostructures made of two promising HC candidate materials (perovskite and vdW materials) beyond the SQ limit[146–148]. Further research on perovskite-based vdW

Auger heating
Auger recombination increases the total energy of carriers, therefore, heating the electronic system.

heterostructures is expected to harness the benefits of HC and CM effects, enhancing the PCE of HCSCs.

Challenges and outlook

In addition to efficient HC generation, spatially confined 2D vdW materials possess extremely efficient CM with quantum yield ~99% when compared with other dimensional semiconductors (0D/1D/3D)[24] (FIG. 8a). Thus, by exclusively considering the HC effect, a maximum V_{OC} may be achieved (V_{OC}^{HC}) when only the CM effect can boost the I_{SC} to the highest point (I_{SC}^{CM}) (FIG. 8b). In a HCSC boosted by CM, the HC energy is partially shared in CM, whereas the remaining HC energy could lead to a high V_{OC} if other HC energy loss pathways are eliminated. Thus, owing to the energy conservation principle, a single HC absorber material cannot drive the HC and CM effects simultaneously up to the extreme point, thereby, limiting the overall PCE (FIG. 8b). An ideal solar cell efficiency can be realized by introducing the materials in tandem to incorporate the HC and CM effects simultaneously (FIG. 8b). Skilfully designed perovskite-based vdW heterostructures consisting of two HC absorber materials could introduce a synergistic HC photovoltaic effect beyond the SQ limit. These systems are rarely investigated for HC carrier effects and, thus, need further attention. Besides, extensive research is ongoing in the field of photovoltaics based on quantum dots[149], nanowires[150], photon upconversion[151,152] and exciton fission[153,154]. Conceptual integration of these systems with vdW heterostructures can be investigated in the future for enhanced PCE[155].

Realization of a suitable candidate for ESCs in a practical HCSC for the efficient extraction of HCs without energy loss still remains a major challenge. Ideally, an ESC comprises a tunnelling barrier and a resonant level (energy-selective level), allowing a very narrow range of energies ($\delta E \ll k_B T$) to flow, whereas the other electrons are bounced back into the HC absorber[29,156]. The highest

energy selectivities are obtained in wide-bandgap semiconductors with narrow valence and conduction bands, such as quantum dots, quantum wells, organic molecules and atomic impurities, enabling a sharp transition and minimized HC cooling during extraction[10,157,158]. The concept of semi-ESCs functioning as a high-pass filter ($\delta E \gg k_B T$) for the HCs is also promising and shows a comparable PCE with the ideal narrow band-pass ESCs[159]. However, a key concern is evaluating whether the HCs harvested at the ESCs are at the expense of cold carriers, which inadvertently exist in the HC absorber layer due to the broadband solar absorption[9]. To resolve this issue, a deeper understanding and a novel strategy for the fabrication of device architecture is necessary, which may further complicate the device structure.

The incident power density of solar radiation on the Earth's surface is ~1 kW m^{-2}, corresponding to a spectrally integrated photon flux of ~10^6 photons cm^{-2} ps^{-1}, which is much lower than the laser irradiation[1]. Thus, a concentrated solar irradiation using special geometry may be useful to tune the HC lifetimes and their mean free path, leading to a high PCE, as demonstrated in Si and GaAs multijunction cells[160,161]. Importantly, tuned hot-phonon bottleneck, band-filling and Auger heating under a high-excitation photon flux significantly enhance the HC temperature and lifetime of halide perovskites and are expected to be the assisting factors in vdW materials as well. However, maintaining the stability of 2D solar cell absorbers and the device is a major challenge under a high concentration of solar irradiation (≥100 suns)[161]. The device architecture must be revised properly to consider the thermal effects without compromising the PCE.

Atomically thin vdW materials suffer from low optical absorption; therefore, surpassing the SQ limit under 1 sun irradiation is challenging. Multilayer vdW materials could be an alternative to increase optical absorption, which may compromise the HC and CM effects.
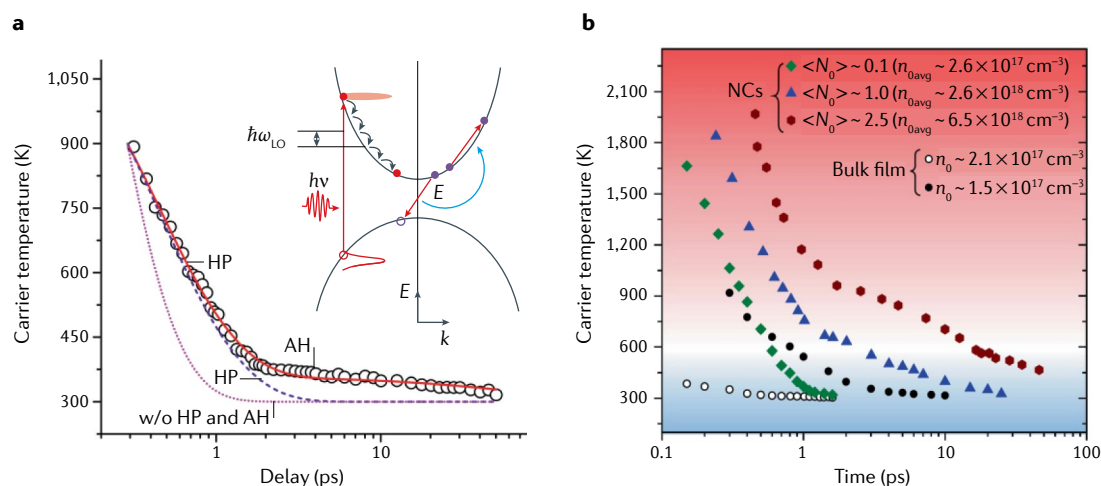
Fig. 7 | **Hot carrier thermalization in perovskite films. a** | Hot carrier cooling dynamics driven by hot phonon (HP) and Auger heating (AH) effects with a pump-photon energy of 2.48 eV at room temperature. Inset: schematic representation of hot electron relaxation pathways via hot-phonon emission (longitudinal optical (LO)) and nonradiative Auger recombination. **b** | Variation of hot carrier temperature with delay time in MAPbBr$_3$ nanocrystals (NCs) of size 8.9 nm and bulk film with various carrier densities. Panel **a** adapted from REF.[141], Springer Nature Limited. Panel **b** adapted from REF.[65], CC BY 4.0 (https://creativecommons.org/licences/by/4.0/).
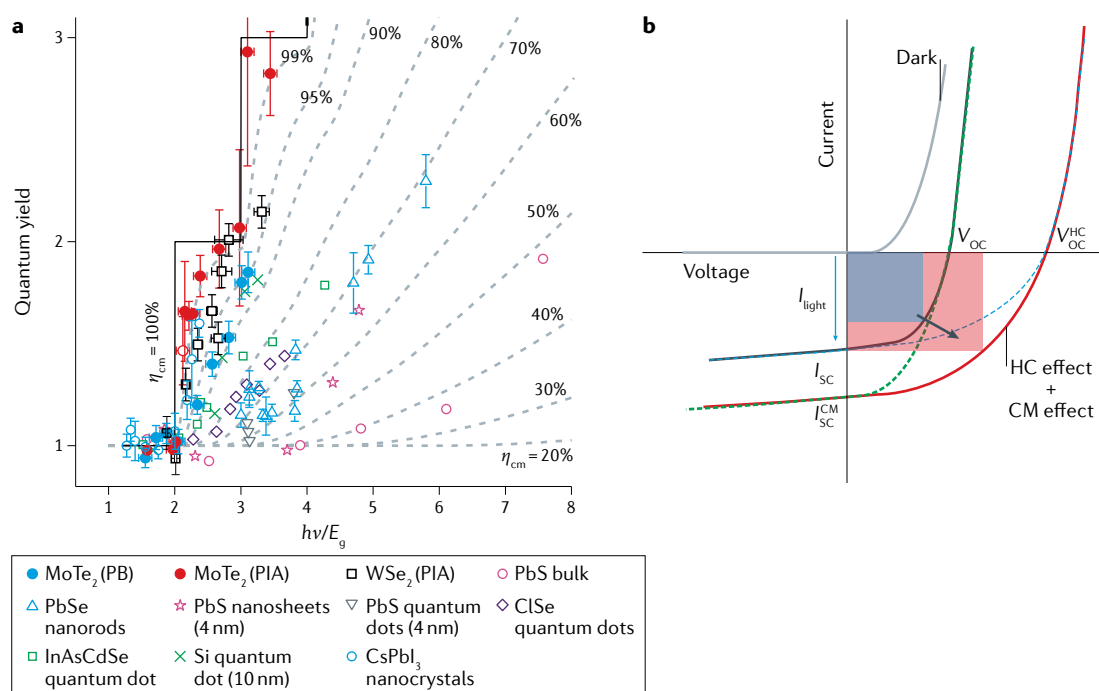
Fig. 8 | **Carrier multiplication and its impact on the solar cell performance, together with the hot carrier effect.**
a | Quantum yield and extracted carrier multiplication (CM) for various nanostructures and bulk materials (0D/1D/2D/3D)[24,46].
b | I–V plot for an ultimate solar cell incorporated with hot carrier (HC) and CM effects. The green arrow indicates a dramatic enhancement in the fill factor of the solar cell performance. PB, photobleaching; PIA, photoinduced absorption. Panel **a** data from REF.[24], Springer Nature Limited; REF.[56], Springer Nature Limited; and REF.[46], ACS.

Thus, it is essential to find a perfect combination of 2D heterojunctions and ESCs for enhanced solar energy harvesting and efficient extraction of HCs, respectively. Furthermore, the CM in 2D vdW materials is observed in a limited spectral range, which restricts its benefits in a practical HCSC driven by broadband solar energy. Additionally, the long-term operational stability of 2D vdW heterojunctions and a complex photovoltaic device in ambient conditions remain a challenge and need further investigation.

Published online 29 January 2021

1. Nelson, C. A., Monahan, N. R. & Zhu, X. Y. Exceeding the Shockley–Queisser limit in solar energy conversion. *Energy Environ. Sci.* **6**, 3508–3519 (2013).
2. Green, M. *Third generation photovoltaics* (eds Kamiya, T., Monemar, B., Venghaus, H. & Yamamoto, Y.) (Springer, 2006).
3. Würfel, P. & Würfel, U. *Physics of Solar Cells: from Basic Principles to Advanced Concepts* 3rd edn (Wiley, 2016).
4. Shockley, W. & Queisser, H. J. Detailed balance limit of efficiency of *p-n* junction solar cells. *J. Appl. Phys.* **32**, 510–519 (1961).
5. Green, M. A., Emery, K., Hishikawa, Y., Warta, W. & Dunlop, E. D. Solar cell efficiency tables (version 41). *Prog. Photovolt. Res. Appl.* **21**, 1–11 (2013).
6. Nozik, A. J. Utilizing hot electrons. *Nat. Energy* **3**, 170–171 (2018).
7. Nozik, A. J. Quantum dot solar cells. *Phys. E Low. Dimens. Syst. Nanostruct.* **14**, 115–120 (2002).
8. Brown, G. F. & Wu, J. Third generation photovoltaics. *Laser Photonics Rev.* **3**, 394–405 (2009).
9. Li, M., Fu, J., Xu, Q. & Sum, T. C. Slow hot-carrier cooling in halide perovskites: prospects for hot-carrier solar cells. *Adv. Mater.* **31**, 1802486 (2019).
10. Conibeer, G. Third-generation photovoltaics. *Mater. Today* **10**, 42–50 (2007).
11. Luque, A. & Martí, A. Increasing the efficiency of ideal solar cells by photon induced transitions at intermediate levels. *Phys. Rev. Lett.* **78**, 5014–5017 (1997).
12. Tauc, J. Electron impact ionization in semiconductors. *J. Phys. Chem. Solids* **8**, 219–223 (1959).
13. Robbins, D. J. Aspects of the theory of impact ionization in semiconductors (I). *Phys. Status Solidi* **97**, 9–50 (1980).
14. McKay, K. G. & McAfee, K. B. Electron multiplication in silicon and germanium. *Phys. Rev.* **91**, 1079–1084 (1953).
15. Beard, M. C., Luther, J. M., Semonin, O. E. & Nozik, A. J. Third generation photovoltaics based on multiple exciton generation in quantum confined semiconductors. *Acc. Chem. Res.* **46**, 1252–1260 (2013).
16. Hanna, M. C., Beard, M. C. & Nozik, A. J. Effect of solar concentration on the thermodynamic power conversion efficiency of quantum-dot solar cells exhibiting multiple exciton generation. *J. Phys. Chem. Lett.* **3**, 2857–2862 (2012).
17. Saeed, S., de Jong, E. M. L. D., Dohnalova, K. & Gregorkiewicz, T. Efficient optical extraction of hot-carrier energy. *Nat. Commun.* **5**, 4665 (2014).
18. Yang, Y. et al. Observation of a hot-phonon bottleneck in lead-iodide perovskites. *Nat. Photonics* **10**, 53–59 (2016).
19. Wen, Y.-C., Chen, C.-Y., Shen, C.-H., Gwo, S. & Sun, C.-K. Ultrafast carrier thermalization in InN. *Appl. Phys. Lett.* **89**, 232114 (2006).
20. Haight, R. Electron dynamics at surfaces. *Surf. Sci. Rep.* **21**, 275–325 (1995).
21. Conibeer, G. J., König, D., Green, M. A. & Guillemoles, J. F. Slowing of carrier cooling in hot carrier solar cells. *Thin Solid Films* **516**, 6948–6953 (2008).
22. Aerts, M. et al. Highly efficient carrier multiplication in PbS nanosheets. *Nat. Commun.* **5**, 3789 (2014).
23. Trinh, M. T. et al. Direct generation of multiple excitons in adjacent silicon nanocrystals revealed by induced absorption. *Nat. Photonics* **6**, 316–321 (2012).
24. Kim, J.-H. et al. Carrier multiplication in van der Waals layered transition metal dichalcogenides. *Nat. Commun.* **10**, 5488 (2019).
    Report of CM in 2D vdW semiconductors.
25. Jeong, I. et al. A tailored TiO₂ electron selective layer for high-performance flexible perovskite solar cells via low temperature UV process. *Nano Energy* **28**, 380–389 (2016).
26. Wang, X. et al. Cerium oxide standing out as an electron transport layer for efficient and stable perovskite solar cells processed at low temperature. *J. Mater. Chem. A* **5**, 1706–1712 (2017).
27. Roose, B. et al. Mesoporous SnO₂ electron selective contact enables UV-stable perovskite solar cells. *Nano Energy* **30**, 517–522 (2016).
28. Jeng, J.-Y. et al. CH₃NH₃PbI₃ perovskite/fullerene planar-heterojunction hybrid solar cells. *Adv. Mater.* **25**, 3727–3732 (2013).
29. Conibeer, G. J. et al. Selective energy contacts for hot carrier solar cells. *Thin Solid Films* **516**, 6968–6973 (2008).
30. Oener, S. Z. et al. Charge carrier-selective contacts for nanowire solar cells. *Nat. Commun.* **9**, 3248 (2018).
31. Adler, D. & Feinleib, J. Electrical and optical properties of narrow-band materials. *Phys. Rev. B* **2**, 3112–3134 (1970).
32. Wu, Y. et al. Thermally stable MAPbI₃ perovskite solar cells with efficiency of 19.19% and area over 1 cm² achieved by additive engineering. *Adv. Mater.* **29**, 1701073 (2017).
33. Rao, H. et al. A 19.0% efficiency achieved in CuOx-based inverted CH₃NH₃PbI₃₋ₓClₓ solar cells by an effective Cl doping method. *Nano Energy* **27**, 51–57 (2016).
34. Zhang, H., Wang, H., Chen, W. & Jen, A. K.-Y. CuGaO₂: a promising inorganic hole-transporting material for highly efficient and stable perovskite solar cells. *Adv. Mater.* **29**, 1604984 (2017).

35. Juarez-Perez, E. J. et al. Role of the selective contacts in the performance of lead halide perovskite solar cells. *J. Phys. Chem. Lett.* **5**, 680–685 (2014).

36. Edri, E. et al. Why lead methylammonium tri-iodide perovskite-based solar cells require a mesoporous electron transporting scaffold (but not necessarily a hole conductor). *Nano Lett.* **14**, 1000–1004 (2014).

37. Jeon, N. J. et al. Solvent engineering for high-performance inorganic–organic hybrid perovskite solar cells. *Nat. Mater.* **13**, 897–903 (2014).

38. Gagliardi, A. & Abate, A. Mesoporous electron-selective contacts enhance the tolerance to interfacial ion accumulation in perovskite solar cells. *ACS Energy Lett.* **3**, 163–169 (2018).

39. del Corro, E. et al. Atypical exciton–phonon interactions in WS$_2$ and WSe$_2$ monolayers revealed by resonance Raman spectroscopy. *Nano Lett.* **16**, 2363–2368 (2016).

40. Chernikov, A. et al. Exciton binding energy and nonhydrogenic Rydberg series in monolayer WS$_2$. *Phys. Rev. Lett.* **113**, 076802 (2014).

41. He, K. et al. Tightly bound excitons in monolayer WSe$_2$. *Phys. Rev. Lett.* **113**, 026803 (2014).

42. Chen, H. et al. Ultrafast formation of interlayer hot excitons in atomically thin MoS$_2$/WS$_2$ heterostructures. *Nat. Commun.* **7**, 12512 (2016).
    A report of ultrafast formation of interlayer hot excitons in 2D vdW heterostructure.

43. Saeed, S. et al. Carrier multiplication in germanium nanocrystals. *Light Sci. Appl.* **4**, e251 (2015).

44. Beard, M. C. et al. Multiple exciton generation in colloidal silicon nanocrystals. *Nano Lett.* **7**, 2506–2512 (2007).

45. Cirloganu, C. M. et al. Enhanced carrier multiplication in engineered quasi-type-II quantum dots. *Nat. Commun.* **5**, 4148 (2014).

46. Padilha, L. A. et al. Aspect ratio dependence of auger recombination and carrier multiplication in PbSe nanorods. *Nano Lett.* **13**, 1092–1099 (2013).

47. Midgett, A. G. et al. Size and composition dependent multiple exciton generation efficiency in PbS, PbSe, and PbS$_x$Se$_{1-x}$ alloyed quantum dots. *Nano Lett.* **13**, 3078–3085 (2013).

48. Brida, D. et al. Ultrafast collinear scattering and carrier multiplication in graphene. *Nat. Commun.* **4**, 1987 (2013).

49. Gabor, N. M., Zhong, Z., Bosnick, K., Park, J. & McEuen, P. L. Extremely efficient multiple electron-hole pair generation in carbon nanotube photodiodes. *Science* **325**, 1367 (2009).
    Report of CM in carbon nanotube p-n junction photodiode.

50. Sukhovatkin, V., Hinds, S., Brzozowski, L. & Sargent, E. H. Colloidal quantum-dot photodetectors exploiting multiexciton generation. *Science* **324**, 1542–1544 (2009).

51. Sambur, J. B., Novet, T. & Parkinson, B. A. Multiple exciton collection in a sensitized photovoltaic system. *Science* **330**, 63–66 (2010).

52. Ellingson, R. J. et al. Highly efficient multiple exciton generation in colloidal PbSe and PbS quantum dots. *Nano Lett.* **5**, 865–871 (2005).

53. Semonin, O. E. et al. Peak external photocurrent quantum efficiency exceeding 100% via MEG in a quantum dot solar cell. *Science* **334**, 1530–1533 (2011).

54. Schaller, R. D., Sykora, M., Jeong, S. & Klimov, V. I. High-efficiency carrier multiplication and ultrafast charge separation in semiconductor nanocrystals studied via time-resolved photoluminescence. *J. Phys. Chem. B* **110**, 25332–25338 (2006).

55. Murphy, J. E. et al. PbTe colloidal nanocrystals: synthesis, characterization, and multiple exciton generation. *J. Am. Chem. Soc.* **128**, 3241–3247 (2006).

56. de Weerd, C. et al. Efficient carrier multiplication in CsPbI$_3$ perovskite nanocrystals. *Nat. Commun.* **9**, 4199 (2018).

57. Cong, M. et al. Carrier multiplication and hot-carrier cooling dynamics in quantum-confined CsPbI$_3$ perovskite nanocrystals. *J. Phys. Chem. Lett.* **11**, 1921–1926 (2020).

58. Bernardi, M., Palummo, M. & Grossman, J. C. Extraordinary sunlight absorption and one nanometer thick photovoltaics using two-dimensional monolayer materials. *Nano Lett.* **13**, 3664–3670 (2013).

59. Polman, A., Knight, M., Garnett, E. C., Ehrler, B. & Sinke, W. C. Photovoltaic materials: present efficiencies and future challenges. *Science* **352**, aad4424 (2016).

60. Tran, M. D. et al. Decelerated hot carrier cooling in graphene via nondissipative carrier injection from MoS$_2$. *ACS Nano* **14**, 13905–13912 (2020).
    A report of prolonged nondissipative interlayer HC transfer in a graphene–MoS$_2$ heterostructure.

61. Yuan, L. et al. Photocarrier generation from interlayer charge-transfer transitions in WS$_2$-graphene heterostructures. *Sci. Adv.* **4**, e1700324 (2018).

62. Liu, W. et al. Approaching the collection limit in hot electron transistors with ambipolar hot carrier transport. *ACS Nano* **13**, 14191–14197 (2019).

63. Wang, L. et al. Slow cooling and efficient extraction of C-exciton hot carriers in MoS$_2$ monolayer. *Nat. Commun.* **8**, 13906 (2017).
    Report of slow cooling and efficient extraction of C-exciton HCs in the MoS$_2$–graphene interface.

64. Xing, G. et al. Long-range balanced electron- and hole-transport lengths in organic-inorganic CH$_3$NH$_3$PbI$_3$. *Science* **342**, 344–347 (2013).

65. Li, M. et al. Slow cooling and highly efficient extraction of hot carriers in colloidal perovskite nanocrystals. *Nat. Commun.* **8**, 14350 (2017).

66. Guo, Z. et al. Long-range hot-carrier transport in hybrid perovskites visualized by ultrafast microscopy. *Science* **356**, 59–62 (2017).

67. Conibeer, G., Nozik, A. J. & Beard, M. C. *Advanced Concepts in Photovoltaics* (RSC, 2014).

68. Moliton, A. *Solid-State Physics for Electronics* (Wiley, 2009).

69. Fara, L. & Yamaguchi, M. *Advanced Solar Cell Materials, Technology, Modeling, and Simulation* 1st edn (IGI Global, 2012).

70. Klemens, P. G. Anharmonic decay of optical phonons. *Phys. Rev.* **148**, 845–848 (1966).

71. Ridley, B. K. Electron scattering by confined LO polar phonons in a quantum well. *Phys. Rev. B* **39**, 5282–5286 (1989).

72. Schaller, R. D. & Klimov, V. I. High efficiency carrier multiplication in PbSe nanocrystals: implications for solar energy conversion. *Phys. Rev. Lett.* **92**, 186601 (2004).

73. Li, M. et al. Low threshold and efficient multiple exciton generation in halide perovskite nanocrystals. *Nat. Commun.* **9**, 4197 (2018).

74. Tisdale, W. A. et al. Hot-electron transfer from semiconductor nanocrystals. *Science* **328**, 1543–1547 (2010).

75. Colvin, V. L., Schlamp, M. C. & Alivisatos, A. P. Light-emitting diodes made from cadmium selenide nanocrystals and a semiconducting polymer. *Nature* **370**, 354–357 (1994).

76. Konstantatos, G. & Sargent, E. H. Nanostructured materials for photon detection. *Nat. Nanotechnol.* **5**, 391–400 (2010).

77. Woggon, U. et al. Ultrafast energy relaxation in quantum dots. *Phys. Rev. B* **54**, 17681–17690 (1996).

78. Klimov, V. I., McBranch, D. W., Leatherdale, C. A. & Bawendi, M. G. Electron and hole relaxation pathways in semiconductor quantum dots. *Phys. Rev. B* **60**, 13740–13749 (1999).

79. Schaller, R. D. et al. Breaking the phonon bottleneck in semiconductor nanocrystals via multiphonon emission induced by intrinsic nonadiabatic interactions. *Phys. Rev. Lett.* **95**, 196401 (2005).

80. Hendry, E. et al. Direct observation of electron-to-hole energy transfer in CdSe quantum dots. *Phys. Rev. Lett.* **96**, 057408 (2006).

81. Pandey, A. & Guyot-Sionnest, P. Slow electron cooling in colloidal quantum dots. *Science* **322**, 929–932 (2008).

82. Miaja-Avila, L. et al. Direct mapping of hot-electron relaxation and multiplication dynamics in PbSe quantum dots. *Nano Lett.* **12**, 1588–1591 (2012).

83. Mak, K. F. et al. Measurement of the optical conductivity of graphene. *Phys. Rev. Lett.* **101**, 196405 (2008).

84. Nair, R. R. et al. Fine structure constant defines visual transparency of graphene. *Science* **320**, 1308 (2008).

85. Winnerl, S. et al. Carrier relaxation in epitaxial graphene photoexcited near the Dirac point. *Phys. Rev. Lett.* **107**, 237401 (2011).

86. Bistritzer, R. & MacDonald, A. H. Electronic cooling in graphene. *Phys. Rev. Lett.* **102**, 206410 (2009).

87. Avouris, P. Graphene: electronic and photonic properties and devices. *Nano Lett.* **10**, 4285–4294 (2010).

88. Castro Neto, A. H., Guinea, F., Peres, N. M. R., Novoselov, K. S. & Geim, A. K. The electronic properties of graphene. *Rev. Mod. Phys.* **81**, 109–162 (2009).

89. Breusing, M. et al. Ultrafast nonequilibrium carrier dynamics in a single graphene layer. *Phys. Rev. B* **83**, 153410 (2011).

90. Tomadin, A., Brida, D., Cerullo, G., Ferrari, A. C. & Polini, M. Nonequilibrium dynamics of photoexcited electrons in graphene: collinear scattering, Auger processes, and the impact of screening. *Phys. Rev. B* **88**, 035430 (2013).

91. Chen, Y., Li, Y., Zhao, Y., Zhou, H. & Zhu, H. Highly efficient hot electron harvesting from graphene before electron-hole thermalization. *Sci. Adv.* **5**, eaax9958 (2019).
    A report of ultrafast hot electron extraction before carrier thermalization in graphene heterostructures.

92. Winzer, T. & Malić, E. Impact of Auger processes on carrier dynamics in graphene. *Phys. Rev. B* **85**, 241404 (2012).

93. Liu, W.-T. et al. Nonlinear broadband photoluminescence of graphene induced by femtosecond laser irradiation. *Phys. Rev. B* **82**, 081408 (2010).

94. Lui, C. H., Mak, K. F., Shan, J. & Heinz, T. F. Ultrafast photoluminescence from graphene. *Phys. Rev. Lett.* **105**, 127404 (2010).

95. Sun, D. et al. Ultrafast relaxation of excited Dirac fermions in epitaxial graphene using optical differential transmission spectroscopy. *Phys. Rev. Lett.* **101**, 157402 (2008).

96. Berciaud, S. et al. Electron and optical phonon temperatures in electrically biased graphene. *Phys. Rev. Lett.* **104**, 227401 (2010).

97. Song, J. C. W., Reizer, M. Y. & Levitov, L. S. Disorder-assisted electron-phonon scattering and cooling pathways in graphene. *Phys. Rev. Lett.* **109**, 106602 (2012).

98. Graham, M. W., Shi, S.-F., Ralph, D. C., Park, J. & McEuen, P. L. Photocurrent measurements of supercollision cooling in graphene. *Nat. Phys.* **9**, 103–108 (2013).

99. Gabor, N. M. et al. Hot carrier–assisted intrinsic photoresponse in graphene. *Science* **334**, 648–652 (2011).

100. Song, J. C. W., Rudner, M. S., Marcus, C. M. & Levitov, L. S. Hot carrier transport and photocurrent response in graphene. *Nano Lett.* **11**, 4688–4692 (2011).

101. Freitag, M., Low, T. & Avouris, P. Increased responsivity of suspended graphene photodetectors. *Nano Lett.* **13**, 1644–1648 (2013).

102. Wei, P., Bao, W., Pu, Y., Lau, C. N. & Shi, J. Anomalous thermoelectric transport of Dirac particles in graphene. *Phys. Rev. Lett.* **102**, 166808 (2009).

103. Xu, X., Gabor, N. M., Alden, J. S., van der Zande, A. M. & McEuen, P. L. Photo-thermoelectric effect at a graphene interface junction. *Nano Lett.* **10**, 562–566 (2010).

104. Koppens, F. H. L. et al. Photodetectors based on graphene, other two-dimensional materials and hybrid systems. *Nat. Nanotechnol.* **9**, 780–793 (2014).

105. Tielrooij, K. J. et al. Generation of photovoltage in graphene on a femtosecond timescale through efficient carrier heating. *Nat. Nanotechnol.* **10**, 437–443 (2015).

106. Paton, K. R. et al. Scalable production of large quantities of defect-free few-layer graphene by shear exfoliation in liquids. *Nat. Mater.* **13**, 624–630 (2014).

107. Williams, K. J., Nelson, C. A., Yan, X., Li, L.-S. & Zhu, X. Hot electron injection from graphene quantum dots to TiO$_2$. *ACS Nano* **7**, 1388–1394 (2013).

108. Kang, M. et al. Universal mechanism of band-gap engineering in transition-metal dichalcogenides. *Nano Lett.* **17**, 1610–1615 (2017).

109. Hunt, R. J., Monserrat, B., Zólyomi, V. & Drummond, N. D. Diffusion quantum Monte Carlo and *GW* study of the electronic properties of monolayer and bulk hexagonal boron nitride. *Phys. Rev. B* **101**, 205115 (2020).

110. Ma, Q. et al. Tuning ultrafast electron thermalization pathways in a van der Waals heterostructure. *Nat. Phys.* **12**, 455–459 (2016).

111. Ju, L. et al. Photoinduced doping in heterostructures of graphene and boron nitride. *Nat. Nanotechnol.* **9**, 348–352 (2014).

112. Huang, L. et al. Ultrafast transient absorption microscopy studies of carrier dynamics in epitaxial graphene. *Nano Lett.* **10**, 1308–1313 (2010).

113. Long, M. et al. Broadband photovoltaic detectors based on an atomically thin heterostructure. *Nano Lett.* **16**, 2254–2259 (2016).

114. Malic, E., Winzer, T., Bobkin, E. & Knorr, A. Microscopic theory of absorption and ultrafast many-particle kinetics in graphene. *Phys. Rev. B* **84**, 205406 (2011).

115. Massicotte, M. et al. Photo-thermionic effect in vertical graphene heterostructures. *Nat. Commun.* **7**, 12174 (2016).

116. Wen, X. et al. Ultrafast probes of electron–hole transitions between two atomic layers. *Nat. Commun.* **9**, 1859 (2018).

117. He, J. et al. Electron transfer and coupling in graphene–tungsten disulfide van der Waals heterostructures. *Nat. Commun.* **5**, 5622 (2014).

118. Urcuyo, R., Duong, D. L., Sailer, P., Burghard, M. & Kern, K. Hot carrier extraction from multilayer graphene. *Nano Lett.* **16**, 6761–6766 (2016). **Proof of concept for HC extraction from graphene**.

119. Wang, F. & Melosh, N. A. Power-independent wavelength determination by hot carrier collection in metal-insulator-metal devices. *Nat. Commun.* **4**, 1711 (2013).

120. Paul, K. K., Mawlong, L. P. L. & Giri, P. K. Trion-inhibited strong excitonic emission and broadband giant photoresponsivity from chemical vapor-deposited monolayer MoS_2 grown in situ on TiO_2 nanostructure. *ACS Appl. Mater. Interfaces* **10**, 42812–42825 (2018).

121. Selcuk, S. & Selloni, A. Facet-dependent trapping and dynamics of excess electrons at anatase TiO_2 surfaces and aqueous interfaces. *Nat. Mater.* **15**, 1107–1112 (2016).

122. Tielrooij, K. J. et al. Photoexcitation cascade and multiple hot-carrier generation in graphene. *Nat. Phys.* **9**, 248–252 (2013).

123. Aeschlimann, S. et al. Direct evidence for efficient ultrafast charge separation in epitaxial WS_2/graphene heterostructures. *Sci. Adv.* **6**, eaay0761 (2020).

124. Froehlicher, G., Lorchat, E. & Berciaud, S. Charge versus energy transfer in atomically thin graphene-transition metal dichalcogenide van der Waals heterostructures. *Phys. Rev. X* **8**, 011007 (2018).

125. Geim, A. K. & Grigorieva, I. V. Van der Waals heterostructures. *Nature* **499**, 419–425 (2013).

126. Lee, C.-H. et al. Atomically thin p–n junctions with van der Waals heterointerfaces. *Nat. Nanotechnol.* **9**, 676–681 (2014). **This paper reports on atomically thin p–n junction photovoltaic devices**.

127. Luong, D. H. et al. Tunneling photocurrent assisted by interlayer excitons in staggered van der Waals hetero-bilayers. *Adv. Mater.* **29**, 1701512 (2017).

128. Wang, S., Khafizov, M., Tu, X., Zheng, M. & Krauss, T. D. Multiple exciton generation in single-walled carbon nanotubes. *Nano Lett.* **10**, 2381–2386 (2010).

129. Malapanis, A., Perebeinos, V., Sinha, D. P., Comfort, E. & Lee, J. U. Quantum efficiency and capture cross section of first and second excitonic transitions of single-walled carbon nanotubes measured through photoconductivity. *Nano Lett.* **13**, 3531–3538 (2013).

130. Aspitarte, L., McCulley, D. R. & Minot, E. D. Photocurrent quantum yield in suspended carbon nanotube p–n junctions. *Nano Lett.* **16**, 5589–5593 (2016).

131. McCulley, D. R., Senger, M. J., Bertoni, A., Perebeinos, V. & Minot, E. D. Extremely efficient photocurrent generation in carbon nanotube photodiodes enabled by a strong axial electric field. *Nano Lett.* **20**, 433–440 (2020).

132. Barati, F. et al. Hot carrier-enhanced interlayer electron–hole pair multiplication in 2D semiconductor heterostructure photocells. *Nat. Nanotechnol.* **12**, 1134–1139 (2017). **Experimental evidence of interlayer CM in a 2D van der Waals heterostructure near room temperature**.

133. Nourbakhsh, A., Zubair, A., Dresselhaus, M. S. & Palacios, T. Transport properties of a MoS_2/WSe_2 heterojunction transistor and its potential for application. *Nano Lett.* **16**, 1359–1366 (2016).

134. Ryan, J. F. et al. Time-resolved photoluminescence of two-dimensional hot carriers in GaAs-AlGaAs heterostructures. *Phys. Rev. Lett.* **53**, 1841–1844 (1984).

135. Nguyen, D.-T. et al. Quantitative experimental assessment of hot carrier-enhanced solar cells at room temperature. *Nat. Energy* **3**, 236–242 (2018).

136. Hirst, L. C., Walters, R. J., Führer, M. F. & Ekins-Daukes, N. J. Experimental demonstration of hot-carrier photo-current in an InGaAs quantum well solar cell. *Appl. Phys. Lett.* **104**, 231115 (2014).

137. Hirst, L. C., Fujii, H., Wang, Y., Sugiyama, M. & Ekins-Daukes, N. J. Hot carriers in quantum wells for photovoltaic efficiency enhancement. *IEEE J. Photovolt.* **4**, 244–252 (2014).

138. Esmaielpour, H. et al. Exploiting intervalley scattering to harness hot carriers in III–V solar cells. *Nat. Energy* **5**, 336–343 (2020).

139. Varghese, A. et al. Near-direct bandgap WSe_2/ReS_2 type-II pn heterojunction for enhanced ultrafast photodetection and high-performance photovoltaics. *Nano Lett.* **20**, 1707–1717 (2020).

140. Richter, J. M. et al. Ultrafast carrier thermalization in lead iodide perovskite probed with two-dimensional electronic spectroscopy. *Nat. Commun.* **8**, 376 (2017).

141. Fu, J. et al. Author Correction: Hot carrier cooling mechanisms in halide perovskites. *Nat. Commun.* **9**, 238 (2018).

142. Yang, J. et al. Acoustic-optical phonon up-conversion and hot-phonon bottleneck in lead-halide perovskites. *Nat. Commun.* **8**, 14120 (2017).

143. Evans, T. J. S. et al. Competition between hot-electron cooling and large polaron screening in $CsPbBr_3$ perovskite single crystals. *J. Phys. Chem. C* **122**, 13724–13730 (2018).

144. Bretschneider, S. A. et al. Quantifying polaron formation and charge carrier cooling in lead-iodide perovskites. *Adv. Mater.* **30**, 1707312 (2018).

145. Kaur, G., Babu, K. J. & Ghosh, H. N. Temperature-dependent interplay of polaron formation and hot carrier cooling dynamics in $CsPbBr_3$ nanocrystals: role of carrier–phonon coupling strength. *J. Phys. Chem. Lett.* **11**, 6206–6213 (2020).

146. Tang, Q., Zhou, Q., Duan, J., Yang, X. & Duan, Y. Interfacial strain release from the WS_2/$CsPbBr_3$ van der Waals heterostructure for 1.7 V voltage all-inorganic perovskite solar cells. *Angew. Chem. Int. Ed.* **59**, 21997–22001 (2020).

147. Cheng, H.-C. et al. van der Waals heterojunction devices based on organohalide perovskites and two-dimensional materials. *Nano Lett.* **16**, 367–373 (2016).

148. Fang, Q. et al. Ultrafast charge transfer in perovskite nanowire/2D transition metal dichalcogenide heterostructures. *J. Phys. Chem. Lett.* **9**, 1655–1662 (2018).

149. Semonin, O. E., Luther, J. M. & Beard, M. C. Quantum dots for next-generation photovoltaics. *Mater. Today* **15**, 508–515 (2012).

150. Krogstrup, P. et al. Single-nanowire solar cells beyond the Shockley–Queisser limit. *Nat. Photonics* **7**, 306–310 (2013).

151. Asahi, S., Teranishi, H., Kusaki, K., Kaizu, T. & Kita, T. Two-step photon up-conversion solar cells. *Nat. Commun.* **8**, 14962 (2017).

152. Huang, Z. et al. Nanocrystal size and quantum yield in the upconversion of green to violet light with CdSe and anthracene derivatives. *Chem. Mater.* **27**, 7503–7507 (2015).

153. Einzinger, M. et al. Sensitization of silicon by singlet exciton fission in tetracene. *Nature* **571**, 90–94 (2019).

154. Bardeen, C. J. Time dependent correlations of entangled states with nondegenerate branches and possible experimental realization using singlet fission. *J. Chem. Phys.* **151**, 124503 (2019).

155. Broch, K. et al. Robust singlet fission in pentacene thin films with tuned charge transfer interactions. *Nat. Commun.* **9**, 954 (2018).

156. König, D. et al. Hot carrier solar cells: Principles, materials and design. *Phys. E Low Dimens. Syst. Nanostruct.* **42**, 2862–2866 (2010).

157. Würfel, P. Solar energy conversion with hot electrons from impact ionisation. *Sol. Energy Mater. Sol. Cell* **46**, 43–52 (1997).

158. Paul, K. K. et al. Strongly enhanced visible light photoelectrocatalytic hydrogen evolution reaction in an n-doped MoS_2/TiO_2(B) heterojunction by selective decoration of platinum nanoparticles at the MoS_2 edge sites. *J. Mater. Chem. A* **6**, 22681–22696 (2018).

159. Le Bris, A. & Guillemoles, J. F. Hot carrier solar cells: achievable efficiency accounting for heat losses in the absorber and through contacts. *Appl. Phys. Lett.* **97**, 113506 (2010).

160. Guter, W. et al. Current-matched triple-junction solar cell reaching 41.1% conversion efficiency under concentrated sunlight. *Appl. Phys. Lett.* **94**, 223504 (2009).

161. Lang, F. et al. Influence of radiation on the properties and the stability of hybrid perovskites. *Adv. Mater.* **30**, 1702905 (2018).

162. Kahmann, S. & Loi, M. A. Hot carrier solar cells and the potential of perovskites for breaking the Shockley–Queisser limit. *J. Mater. Chem. C* **7**, 2471–2486 (2019).